From rifting to oceanization in the Gulf of Aden: Insights from 2D numerical models

Arcangela Bollino [*], Alessandro Regorda, Roberto Sabadini, Anna Maria Marotta

Università degli Studi di Milano, Department of Earth Science, L. Cicognara 7, 20129 Milano, Italy

ABSTRACT

We investigate the evolution of the Gulf of Aden from rift initiation to the development of active oceanic spreading center by means of 2D thermo-mechanical numerical models, in which the formation of oceanic crust and serpentinite due to the hydration of the uprising mantle peridotite has been implemented. Our analysis highlights that evolution of the models is characterized by four main tectonic phases: a) a first phase (phase I) characterized by low deformation rates throughout the divergent crustal blocks, except near the future ridge where a high crustal velocity gradient generates an intense strain rates; b) a second phase (phase II) during which the crust undergoes an intense, stable and widespread strain, with the localization of the thinning near the future ridge that ends into crustal breakup c) a third phase (phase III) that characterizes the post- crustal breakup evolution of the models during which a mechanical relaxation of the system and a continuum decreasing of the strain rate can be observed, until the occurrence of lithospheric breakup, and d) fourth phase (phase IV) that lasts up to the end of the evolution and during which the two continental blocks move rigidly. We also find that the timing of mantle serpentinization is not affected by the initial thermal configuration of the lithosphere, but a relationship with the crustal thickness can be observed. Rather, the timing of mantle partial melting strongly depends on the initial thermal conditions of both the lithosphere and the crust. We constrain the crustal and lithospheric thickness at 40 and 150 km, respectively, considering the timing of breakup that occurs 20 Myr after the onset of the extension for 0.05% percentage of mantle hydration (in agreement with magma-poor rift margins). Finally, model prediction supports the hypothesis that the Gulf of Aden developed as a slow passive rift of a thin lithosphere with a thick crust and the variation of the features along the passive margins could be related to a lateral variation in the amount of H_2O in the mantle, which determines different timing in the mantle melting.

1. Introduction

Discriminating the driving forces that control the complex tectonic context in the Gulf of Aden and surrounding areas is one of the most recent and intriguing topics for researchers who study the evolution of the area surrounding the Afar Depression. The main mechanisms proposed to date are a) far-field tensile tectonic forces due to the subduction of the Tethyan slab below the Zagros suture zone (e.g., Bellahsen et al., 2003), b) emplacement of the African plume that may have caused diffuse lithospheric weakening (e.g., Bellahsen et al., 2003) and c) a combination of these mechanisms (e.g., Petrunin et al., 2020).

Several analogue and numerical models have been developed in recent years that focus on different aspects, such as the role of the subduction-collision process on Arabia-Africa separation and on intraplate stresses, which generated the Red Sea-Gulf of Aden rift system (Bellahsen et al., 2003); the effect of oblique rifting on the fault geometry (Autin et al., 2010, 2013); the reactivation of preexisting faults and rift localization (Bellahsen et al., 2006) and their roles in controlling the geometry and the kinematics of rifts (Autin et al., 2013); interactions between local and far-field tectonic stresses in an evolving rift system (Brune and Autin, 2013); the importance of mantle strength (Gueydan et al., 2008), rheology and composition on the formation of passive margins, ocean-continent transition zones and oceanic basins (Watremez et al., 2013); the structural consequences of crustal necking processes and of the degree of mechanical decoupling during a relatively continuous extensional event (Chenin et al., 2018); the influence of erosion/sedimentation on the rifting process (Beucher and Huismans, 2020); and the overall effect of inherited obliquity and changes in

relative plate motions along continent-ocean transform margins (Farangitakis et al., 2020). However, many questions remain debated, such as the timing and nature of the rifting and why the ocean-continent transition zone did not develop along the entire oceanic margins.

To shed light on these issues, we implemented a set of numerical models that simulate the passive rifting of lithosphere with varying crustal thickness and initial thermal configuration, whose predictions in terms of timing and petrological characteristics of the phases of rifting make it possible to discriminate among different tectonic hypotheses. Models are founded on integrated modeling of elevation, geoid data and thermal analysis and account for the present-day kinematics observed between the Arabian plate and Africa (Nubia) and Somalia. Rather than being interested on ridge propagation mode as a function of ridge parallel inflow or obliquity, requiring a 3D modeling formulation as for Jourdon et al. (2020) or on the effects of a 3D weak zone in the lower crust as for Liao and Gerya (2015), we are herein interested on the timing of occurrence of oceanization and serpentinization which makes a 2D formulation the preferred one. This 2D formulation allows us to focus on the basic physics of the rifting processes along transects perpendicular to the ridge, focusing the analysis on the central portion of the Gulf of Aden, encompassed between the Shukra-el-Sheik fracture zone and Alula-Fartak fracture zone, which is in fact a 2D structure. Furthermore, within our 2D formulation we implement the formation of oceanic crust by partial melting and magma crystallization, generally not considered in 3D formulations.

2. Tectonic setting

The Gulf of Aden is a young oceanic basin situated between southern Arabia and the Horn of Africa that links the Ethiopian rift and the Red Sea with the Carlsberg Ridge in the NW Indian Ocean.

The rifting started at approximately 40–35 Ma (Watchorn et al., 1998; Watremez et al., 2011), followed by oceanic spreading at approximately 19–18 Ma at the Sheba Ridge, in the eastern part of the Gulf (Bosworth et al., 2005; Watremez et al., 2011; Shuler and Nettles, 2012; Bosworth, 2015). Later, the ridge propagated westward into the central Gulf of Aden by 16 Ma and, at 10 Ma, over 300 km from the central Gulf of Aden to the Shukra al Sheik discontinuity (Bosworth et al., 2005; Bosworth, 2015). Rifting stalled there and propagated west of the Shukra-el-Sheik discontinuity only during the last 2–3 Ma (Shuler and Nettles, 2012). The age of the oceanic crust thus becomes progressively younger westward. The spreading rate increases from 13 mm/yr in the west to ~23 mm/yr in the east (ArRajehi et al., 2010; Autin et al., 2010).

The general trend of the Gulf of Aden is WSW–ENE (N70°E) while the present-day spreading direction ranges between N25°E to the east and N35°E to the west, indicating an oblique rifting (Huchon and Khanbari, 2003).

The oceanic domain of the gulf may be divided into three sectors (western, central and eastern sectors, Fig. 1) by the Shukra-el–Sheik Fracture Zone (SSFZ), the Alula-Fartak Fracture Zone (AFFZ) and the Socotra-Hadbeen Fracture Zone (SHFZ) (Leroy et al., 2010). The eastern sector (light red area in Fig. 1) extends from the Alula-Fartak transform fault to the eastern border of the African craton (Leroy et al., 2012) and shows an extremely thin transitional crust at the Ocean-Continent Transition (OCT), which most likely involves exhumed serpentinized mantle rocks indicating a magma-poor setting (Leroy et al., 2012). The central sector (light yellow area in Fig. 1) of the Gulf lies between the SSFZ and the AFFZ (Leroy et al., 2012) and, as in the eastern sector, the margins here are thought to be either magma-poor, or of intermediate-type, as no magmatic structures, such as seaward-dipping reflectors have been recognized in the OCT. In fact, Nonn et al. (2019) propose that the central Gulf of Aden is composed of hybrid margins (or intermediate-type, Larsen et al., 2018), transitional between magma-rich and magma-poor margins, in the western and eastern parts of the central sector, respectively. Their analysis of marine geophysical and geological
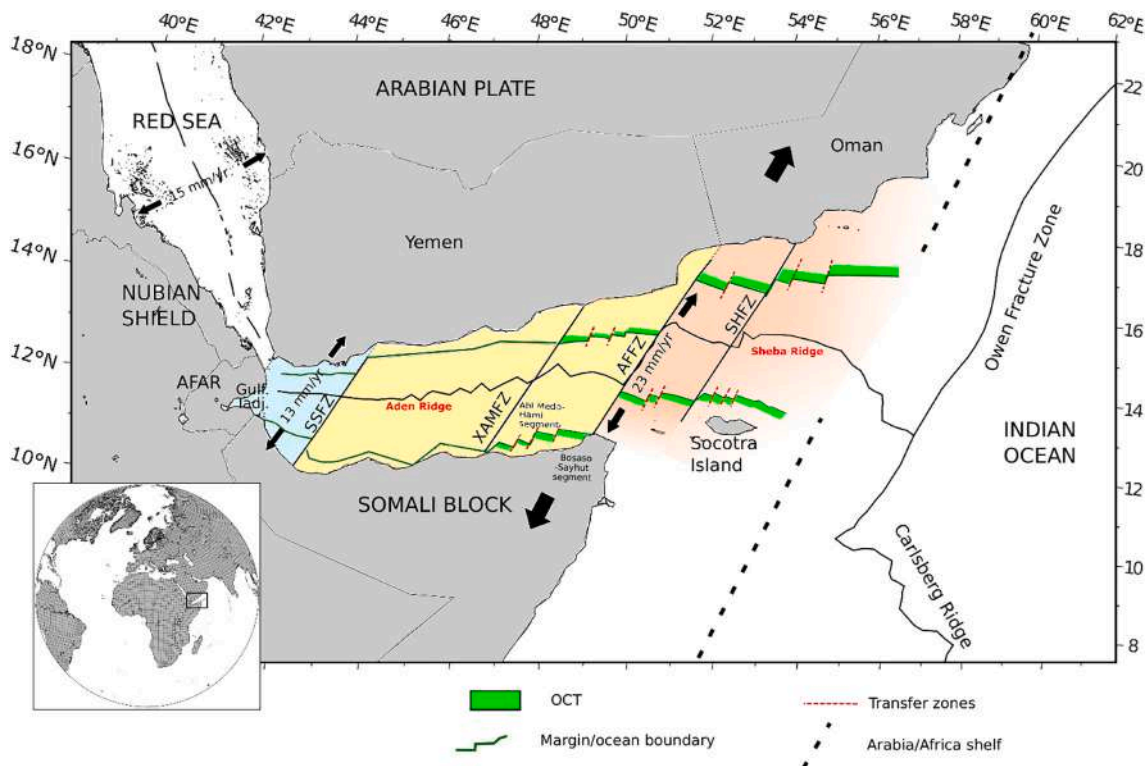

Fig. 1. Overview map showing the main tectonic features of the Gulf of Aden and surrounding areas using published data (Leroy et al., 2012; Nonn et al., 2019). Large black arrows indicate the directions of plate motion in the region. SSFZ: Shukra-el-Sheik fracture zone. XAMFZ: Al Mukalla fracture zone. AFFZ: Alula-Fartak fracture zone. SHFZ: Socotra-Hadbeen fracture zone. Cyan, light yellow and light red colors indicate the western, central and eastern sectors, respectively. (For interpretation of the references to colour in this figure legend, the reader is referred to the web version of this article.)

data reveals that at the western boundary of central sector, near the XAMFZ, magmatic processes are predominant and the higher thermal regime is associated with the development of SDRs wedges from the late phase of the thinning of the continental crust (early Miocene- ~ 21 Ma) up to the exhumation phase (Burdigalian- ~ 18 Ma) that lead to the OCT development. East of BHFZ, the Bosaso-Sayhut margins segment is characterized by magma-poor margins for which the exhumation stage is characterized by the unroofing of mantle along multiple detachment faults in the OCT and shortly followed by diachronous volcanism (~18 Ma) (Nonn et al., 2019). The OCT on the northern margin of the central sector is wider in the eastern segment (~23–45 km) than in the western segment (~17–33 km), and on the southern margin, it is wider in the Bosaso-Sayhut segment (~23 km) than in the Ahl-Medo-Hami segment (~10–20 km) (Nonn et al., 2019). The difference in width of the conjugate OCT highlights the asymmetry of the Yemeni and Somalian margins (Nonn et al., 2019).

The western sector (cyan area in Fig. 1) extends from the active rift of the Gulf of Tadjoura to the SSFZ (Leroy et al., 2012). West of the SSFZ, the system was heated up by the strong influence of the Afar plume, which led to breakup with much less extension, inducing the development of volcanic rifted margins in the western part of the Gulf of Aden (Leroy et al., 2012). In fact, the major discontinuity of Shukra-el-Sheik (Fig. 1) may indicate the limit of the Afar plume influence and corresponds to a major change in the rheology of the lithosphere (Basuyau et al., 2010).

3. Conceptual model

3.1. Model setup

The physics of the crust–mantle system during the transition from rifting to seafloor spreading is described by the equations of conservation of mass, momentum and energy for incompressible fluids:

$$\nabla \cdot \boldsymbol{u} = 0 \tag{1}$$

$$-\nabla p + \nabla \cdot \boldsymbol{\tau} + \rho \boldsymbol{g} = 0 \tag{2}$$

$$\rho C_p \left(\frac{\partial T}{\partial t} + \boldsymbol{u} \cdot \nabla T \right) = \nabla \cdot (K \nabla T) + H \tag{3}$$

where **u** is the velocity, p is the pressure, $\boldsymbol{\tau}$ is the deviatoric stress, ρ is the density, $\boldsymbol{g}$ is the gravitational acceleration, C_p is the heat capacity at constant pressure, T is the temperature, K is the thermal conductivity and H is the total internal heating per unit mass.

Eqs. (1), (2) and (3) are integrated using the 2D finite element code SubMar (Marotta et al., 2006) in a 1400 km-wide and 700 km-deep rectangular domain (Fig. 2).

The domain is discretized by a non-deforming irregular grid composed of 5836 quadratic triangular elements and 11,889 nodes. The sizes of the elements vary, with the highest nodal density localized near the future rifting zone, where the most significant gradients in temperature and velocity fields are expected. SubMar uses the streamline upwind/Petrov-Galerkin method to integrate the equation for the conservation of energy and the penalty function formulation (Sewell, 1982) to solve for pressure p:

$$p = -\lambda \left(\frac{\partial u}{\partial x} + \frac{\partial v}{\partial y} \right)$$

where λ is the penalty parameter, chosen to be large enough to guarantee a small change in volume so that the fluid can be considered almost incompressible. We assumed $\lambda = \mu \sqrt{r_p}$, where r_p represents the machine precision and μ is the bulk viscosity (Hughes et al., 1979; Donea and Huerta, 2003; Marotta et al., 2006; Thieulot, 2014).
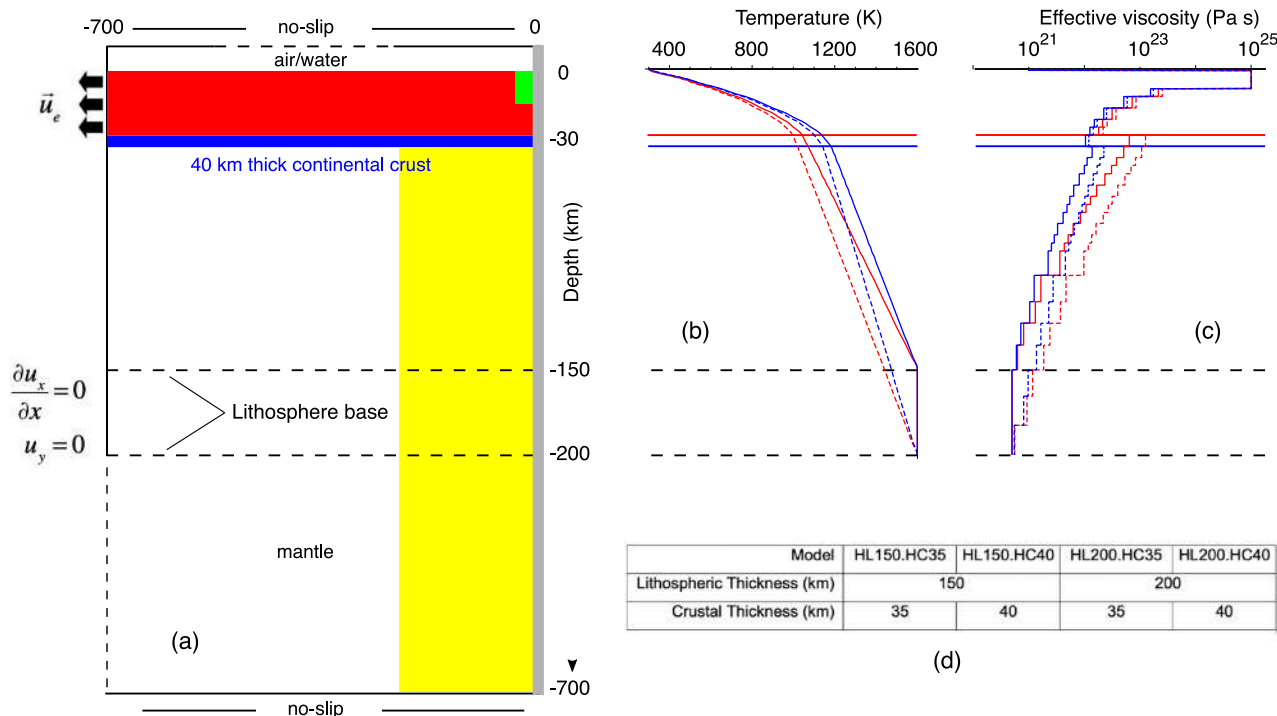

Fig. 2. (a) 2D geometry and numerical setup of the numerical model. Crustal markers are colored red and blue. Mantle markers are colored yellow. Green area indicates the assumed low viscosity weak zone. Thermal (b) and rheological (c) profiles at the beginning of evolution for the models listed in panel d. Blue and red colors in panels (b) and (c) refer to a 40 km and 35 km thick crust, respectively. The thin red and blue lines refer to the geotherms (panel b) and the effective viscosities (panel c) for the 35 km and the 40 km -thick crust models, respectively. Continuous and dashed lines indicate geotherms and effective viscosities for a 150 km and 200 km -thick lithosphere, respectively. The horizontal black dashed lines indicate the base of the 150 and 200 km lithosphere. The horizontal thick solid lines indicate the base of the 35 km (red) and 40 km (blue) -thick crust. (For interpretation of the references to colour in this figure legend, the reader is referred to the web version of this article.)

The marker in-cell technique (e.g., Christensen, 1992) is used to compositionally differentiate the different types of materials with 514,009 markers spatially distributed with a density of 1 marker per 0.25 km^2, identifying through a specific index the material particles of air/water, continental crust, non-serpentinized and serpentinized mantle. Mantle markers have been distributed only along a 200 km-wide vertical column centered at the future ridge position (yellow zone in Fig. 2a). This permitted to assure a high marker concentration and, at same time, to limit the total number of markers and optimize the time consuming. Such marker distribution resulted appropriate to identify those markers involved in the processes under study. During the evolution of the system, each marker is advected using a 4th-order (both in time and in space) Runge–Kutta scheme. Based on the number of markers of type i that reside at each time within each element e, N_i^e, each weighted average elemental property P_e can be defined as follows:

$$P^e = P_m \left[1 - \sum_i \frac{N_i^e}{N_0^e} \right] + \sum_i P_i \frac{N_i^e}{N_0^e}$$

where P_m and P_i are the values of the properties for the mantle and for any particles of type i, respectively, and N_i^e is the maximum number of particles of any type that element e may contain. Regarding the elemental density ρ^e, we assume that it depends on only temperature and composition via the extended Boussinesq approximation in the following form:

$$\rho^e = \rho_m \left[1 - \sum_i \frac{N_i^e}{N_0^e} \right] + \sum_i \rho_i \frac{N_i^e}{N_0^e}$$

where ρ_i is the density of the non-mantle materials (depending only on composition) and $\rho_m = \rho_0 [1 - \alpha(T - T_0)]$ is the mantle density, with reference density ρ_0 at reference temperature T_0.

We assume a visco-plastic behavior for the lithosphere and a viscous behavior for the sub-lithosphere mantle.

The viscous behavior is accounted through an assumed reference viscosity μ_0 in the whole system, and the elemental effective viscosity is calculated as follows:

$$\mu^{eff} = \mu_{viscous} = \mu_{0,i} exp \left[\frac{E_i}{R} \left(\frac{1}{T} - \frac{1}{T_0} \right) \right]$$

where for each material i, $\mu_{0,i}$ is the reference viscosity at temperature T_0 and E_i is the activation energy.

In order to limit the maximum effective viscosity and to minimize the hardening effects of temperature and strain, we introduce a cut-off value of 10^{25} Pa·s, in agreement with other authors (e.g., Gerya and Yuen, 2003, Marotta et al., 2009) (Fig. 2c). Neither stress hardening nor stress softening is considered. This simple rheological model is appropriate in reproducing the average continuum properties of a discontinuous medium and makes the analyses of gross mechanical behavior during the geodynamic evolution of the study area possible, allowing the formation of localized shear zones that can be interpreted as faults in continuum mechanics (see section 4.1).

The numerous models developed to analyze the dynamics of rifting (e.g., Huismans and Beaumont, 2002, 2003; Richter et al., 2021) show that a use of a more complex elasto-visco-plastic rheology affects mainly the initial stages of rifting, when the mode of small-scale localization of deformation structures is important for the successive breakup development. However, this is beyond the scope of the present study, in which we assume an a-priori weakness point where breakup will develop. In particular, we introduced a 10 km wide x 15 km deep weak zone in the center of the model, from surface downward (green area in Fig. 2, panel a), and characterized by a viscosities of 10^{19} Pa·s to localize the deformation and allow the development of the rifting since a continuous medium necessitates a heterogeneity in the mechanical properties as a seed for initiating the process of rifting (Huismans and Beaumont, 2003;

Liao and Gerya, 2015; Wenker and Beaumont, 2018).

We account for the brittle behavior of the crust only to define the rheological condition for mantle serpentinization during continental rifting and the transition to oceanic spreading. Table 1 lists the material and rheological parameters used in the analysis.

In agreement with studies on the lithospheric structure in the Gulf of Aden and its surroundings, four model sets have been developed changing the initial thickness of the continental crust (fixed at 35 and 40 km) and the initial thickness of the lithosphere (fixed at 150 and 200 km), in order to match the lower and upper bounds of the estimates of the present-day crustal and lithospheric thickness in the internal part of the Arabian plate suggested by integrated modeling of elevation, geoid data and thermal analysis (e.g. Hansen et al., 2007; Leroy et al., 2010; Globig et al., 2016). We list the acronyms and setup of the models in Fig. 2d where HL stands for lithospheric thickness and HC stands for crustal thickness.

To allow for topographic variations, a 10 km-thick layer of sticky air is present above the crust, characterized by a viscosity of 10^{20} Pa·s and a density of 1 kg m^{-3} (e.g., Crameri et al., 2012; Marotta et al., 2020). Our topography is thus the surface defined through the envelope of the topmost markers.

We are aware that the limited height of the sticky air could affect to some extent the detailed estimate of the topography, that is not in any case the focus of the present work.

Boundary conditions are fixed in terms of temperature and velocity. The temperature is fixed to 300 K at the top of the crust and through the air layer. A temperature of 1600 K is fixed at the bottom of the model; zero thermal flux occurs through the vertical sidewalls. The initial thermal configuration corresponds to a steady-state conductive thermal profile, from 300 K at the surface to 1600 K at the base of the lithosphere and considering a radiogenic heat production in the continental crust (Table 1); an initial uniform temperature of 1600 K is assumed through the sublithospheric mantle (Fig. 2b). The 1600 K isotherm defines the base of the thermal lithosphere throughout the evolution of the system.

To simulate the northeastward relative motion between the Arabian plate and the African (Nubian) and Somalian plates, we apply an extension rate of 11.5 mm/yr on both sides of the domain, from depths of 0 to 100 km, resulting in symmetric passive rifting with a total extension rate of 23 mm/yr that is compatible with the highest velocities suggested for the eastern part of the Gulf of Aden (ArRajehi et al., 2010; Reilinger et al., 2015). No-slip conditions are prescribed along the top and the bottom of the model domain. Along the vertical sides, from the base of the lithosphere (−100 km) below, we fix to zero the vertical component of velocity and the horizontal gradient of the horizontal component of velocity, according to eq. 1 (Fig. 2a). We ran the simulation for 40 Ma to cover the entire time span (approximately 35–40 Ma) from the beginning of continental rifting to the present (Bosworth et al., 2005; Bellahsen et al., 2006; Leroy et al., 2012; Bosworth, 2015; Rasul et al., 2015; Brune and Autin, 2013). A constant time step of 50 kyr is used that always satisfies the Courant-Friedrichs-Lewy condition.

Table 1
List of the compositional and rheological parameters used in the present analysis (Regorda et al., 2021 and references therein).

	Continental crust	Oceanic crust	Dry mantle	Serpentinized mantle
Rheology	Dry Granite	Diabase	Dry Dunite	–
E (kJ mol^{-1})	123	260	444	–
μ_0 (Pa s)	3.47×10^{21}	1.61×10^{22}	5.01×10^{20}	10^{19}
ρ_0 (kg/m^3)	2640	2961	3200	3000
K (W m^{-1} K^{-1})	3.03	2.1	4.15	4.15
H$_r$ (μW m^{-3})	2.5	0.4	0.002	0.002

3.2. Mantle serpentinization and oceanization

The role of serpentinization of the lithospheric mantle during continental rifting and the transition to oceanic spreading have been extensively discussed in the literature (e.g., Pérez-Gussinyé et al., 2006; Marotta et al., 2018). In the present work, we implement mantle serpentinization and the associated compositional and rheological changes following Marotta et al. (2018)'s approach. At each time step, we check whether a) the pressure and the temperature of each mantle-type marker match the stability field of serpentine and b) the overlying crustal layer is under brittle conditions. For the latter, we use a simplified formulation of Byerlee's law criterion to compute the brittle strength:

$\sigma_{Brittle} = \beta \bullet y$, where $\beta = 16 MPa\ km^{-1}$ and y is the depth, and the brittle strength is compared with the temperature- and pressure-based plastic strength:

$Regime = min\{\sigma_{Brittle}, \sigma_{Plastic}\}$

In our model partial melting of asthenospheric mantle allows the growth of the oceanic crust at the ridge, assuming an instantaneous transfer of mantle melt to shallow depths, as commonly implemented (e. g. Gerya, 2013; Nikolaeva et al., 2008; Gulcher et al., 2019). This is also in agreement with estimates of the magma ascent rate across the continental and oceanic crust (Clague, 1987; Turner et al., 2000).

To verify whether the predicted thermal state can result in partial melting of the mantle and the formation of oceanic crust, we estimate the melting percentage of lithospheric mantle following the melting model by Katz et al. (2003) at each time step, as discussed in Roda et al. (2018). Basuyau et al. (2010) have combined seismological data with existing gravity data in a joint inversion scheme to estimate both *P* wave velocity and density structure beneath the northeastern margin of the Gulf of Aden, reaching depths of 250 km with a spatial resolution of about 50 km. They discuss the presence of anomalous bodies in terms of interaction between mantle and crustal processes, rift evolution and margin/ridge segmentation.

The analysis of joint inversion of gravity and teleseismic data shows evidence for partial melting (3–6%) at a depth of between 60 and 200 km beneath the northern margin in the Southern Oman area along the prolongation of the AFFZ and the SHFZ. In the partial melting implementation, we estimate the melting percentage of lithospheric mantle and we use the value of 3% of partial melting as the minimum value at which the oceanic crust begins to form. This value is also in agreement with melt extraction threshold by Nikolaeva et al. (2008). After the melt fraction reach the threshold the melt is extracted and it migrates instantaneously creating new oceanic crust (Gerya, 2013).

Some authors (Nichols et al., 2002; Thompson et al., 2015) have proposed that the percentage of water near an oceanic ridge tends to increase as the ridge approaches a plume. In proximity to plumes, mid-ocean ridge basalts (MORB) can have H_2O percentages up to 0.03–0.1%, similar to those observed in oceanic island basalts (OIB) (Dixon et al., 2002; Hirschmann, 2006). This feature can also be observed in the central and eastern parts of the Gulf of Aden, where basalts show the geochemical signature of normal MORB (N-MORB) (Rooney et al., 2014; Shinjo et al., 2015) incorporating a component from a plume-associated source. Therefore, we considered the solidus of a wet lherzolite with a bulk of H_2O between 0.05 and 0.1%. We calculate the areas where partial melting occurs at the post-processing stage and the rate of the partial melting is determined following Katz et al. (2003). Within this work, we refer to crustal breakup when the two continental crusts are compositionally separated, although crust can still deform, being still subjected to the shear stresses exerted by the underlying lithospheric mantle which has not yet broken. We assume that lithosphere breakup is instead achieved when the effective strain rate decreases below the threshold value of $10^{-16}\ s^{-1}$ through the whole crustal thickness. The analysis of variations with time in the horizontal velocity and in the strain rate at crustal levels will thus allow to identify the times when crustal and lithospheric breakup occur.

The domain between the thinned continental crust and the oceanic crust, composed of denuded mantle that has been serpentinized before the occurrence of the gabbros, will be henceforth referred to as the Ocean Continent Transition zone (OCT). The width changes of the OCT and of the oceanic lithosphere in the study domain will be estimated considering the structural configuration of the system at the time of partial melting and at the time when the two continents are separated by a distance of 350–400 km (as observed in the Gulf of Aden).

4. Model results

4.1. Thermomechanical evolution and deformation

During the first few million years from the beginning of extension, for all models, the predicted velocity field is controlled mainly by the far-field traction that induces predominantly horizontal velocities throughout the lithosphere. During this stage, the intensity of upwelling mantle flow below the future ridge is lower than the far-field intensity (panels a_2 and b_2 of Figs. 3 to 6), especially for the colder and thus stiffer models HL200.HC35 (Fig. 5) and HL200.HC40 (Fig. 6). With the progression of the forced extension, all models undergo continuous warming that is localized around the position of the future ridge, as revealed by the rising of the 800 K and 1500 K isotherms (Figs. 3 to 6). Thermal thinning is accompanied by progressive crustal thinning, which results in crustal breakup over a period ranging from 6 Ma for model HL150. HC35 to 20 Ma for model HL150.HC40.

The analysis of variations with time in the horizontal velocity and in the strain rate at crustal levels allows us to identify the times when crustal breakup occurs. To aid this analysis, Fig. 7 shows the horizontal crustal velocity, averaged over the crustal thickness, as a function of distance from the future ridge and at different times of evolution.

Four main phases can be distinguished in the thermomechanical evolution of the crust. The first phase (phase I) lasts a few million years from the beginning of extension. During this phase, the horizontal crustal velocities predicted by all models slowly decrease from the external borders to approximately 100 km from the future ridge, while in the central part of the domain the velocities rapidly decrease to 0 mm/yr (Figs. $3a_2$, $4a_2$, $5a_2$ and $6a_2$ and green area in Fig. 7). This velocity pattern induces low strain rates within the crust away from the ridge (ranging from 1 to $3 \cdot 10^{-16}\ s^{-1}$), while the highest values of strain rate (higher than $10^{-14}\ s^{-1}$) characterize the surroundings of the future ridge (Figs. $3a_1$, $4a_1$, $5a_1$ and $6a_1$). This phase lasts 5.9 Ma for model HL150. HC35 (Fig. $3c_1$), 2.9 Ma for model HL150.HC40 (Fig. $4b_1$), 4.9 Ma for model HL200.HC35 (Fig. $5b_1$) and 3.9 Ma for model HL200.HC40 (Fig. $6b_1$), indicating a longer duration of phase I for thinnest crust and thinnest lithosphere.

During the second phase (phase II), a significant change occurs in the horizontal crustal velocities, which linearly decrease in intensity from the borders to the future ridge (Fig. 7), resulting in more intense strain rates, higher than $10^{-15}\ s^{-1}$, throughout the crust. The duration of the second phase is different for the different models. It lasts approximately 17 Ma for model HL150.HC40, 8.5 Ma for models HL200.HC35 and 9.5 Ma for model HL200.HC40 (Figs. 4c, 5c and 6c, respectively), while the HL150.HC35 model does not show a phase II.

The crustal horizontal velocities remain stable until the end of phase II when continental crust breakup occurs. For all models, crustal breakup can be recognized in Fig. 7 by the interrupted dotted black line localized around the future ridge and the immediately preceding velocity profile (black thick solid line). Crustal breakup occurs between 5.9 and 6.4 Ma for model HL150.HC35, between 19.9 and 20.4 Ma for model HL150.HC40, and between 13.4 and 13.9 Ma for models HL200. HC35 and HL200.HC40. Crustal strain rates and horizontal velocity patterns at these two times are shown in Figs. $3c_1$–d_1, $4c_1$–d_1, $5c_1$–d_1 and $6c_1$–d_1 for models HL150.HC35, HL150.HC40, HL200.HC35 and HL200.HC40, respectively. The thermomechanical evolution of model HL150.HC35 is faster than those of the other models, and continental
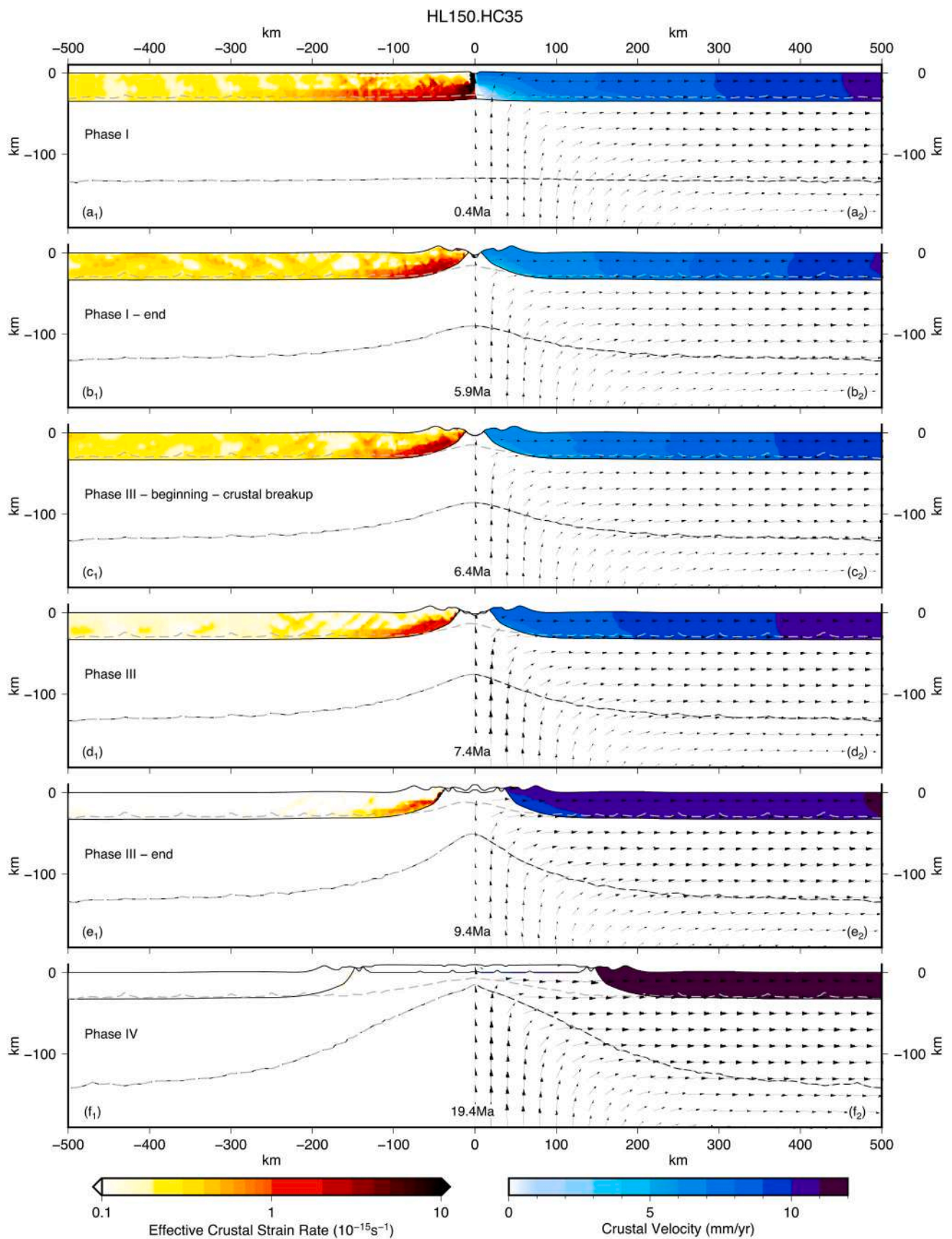
Fig. 3. Effective crustal strain rate (left side) and intensity of crustal horizontal velocity and velocity fields (right side) predicted by model HL150.HC35 at different times after the beginning of forced extension. Gray dashed lines correspond to the 800 K and 1500 K isotherms. Solid black lines represent the envelopes of crustal- and mantle-type markers.
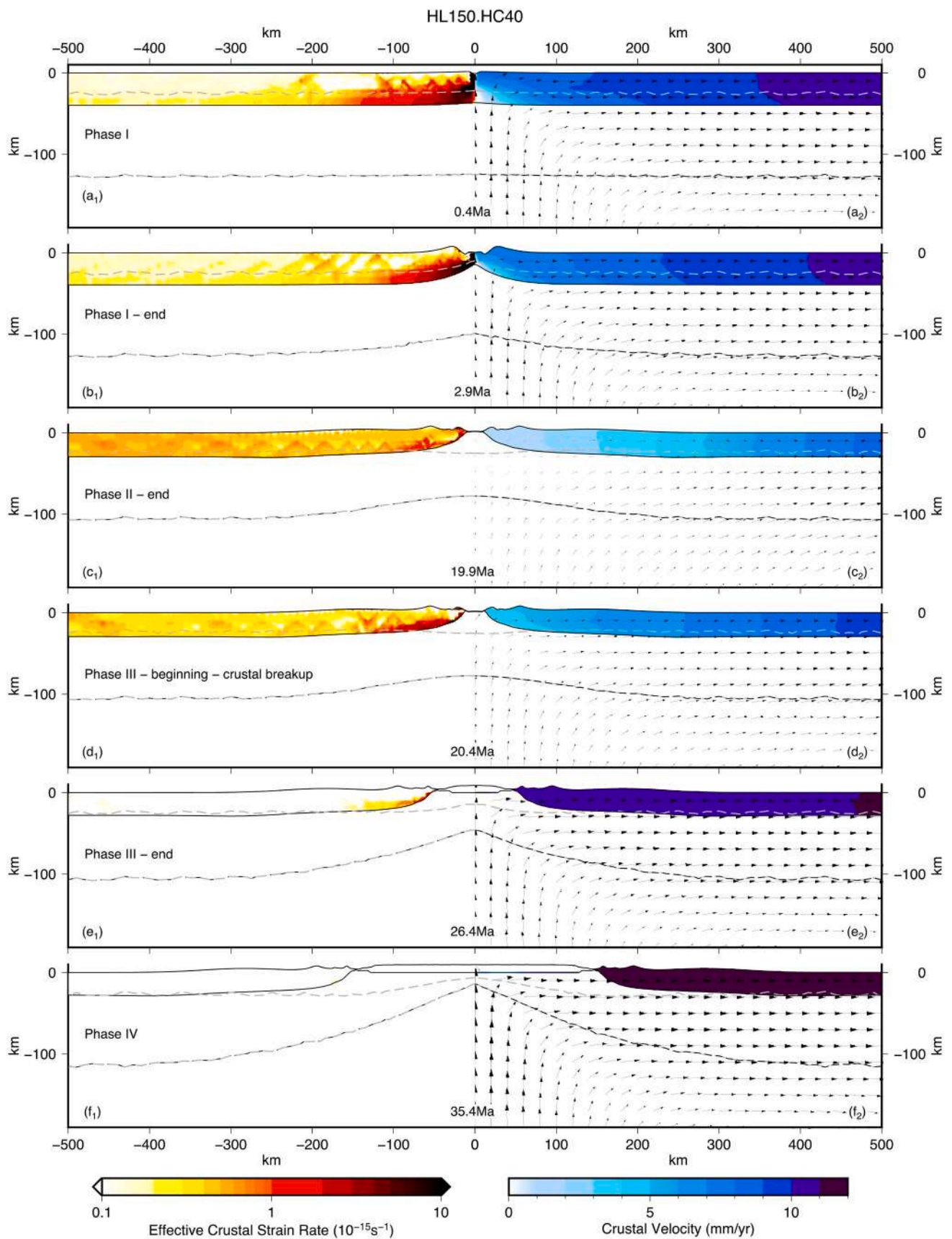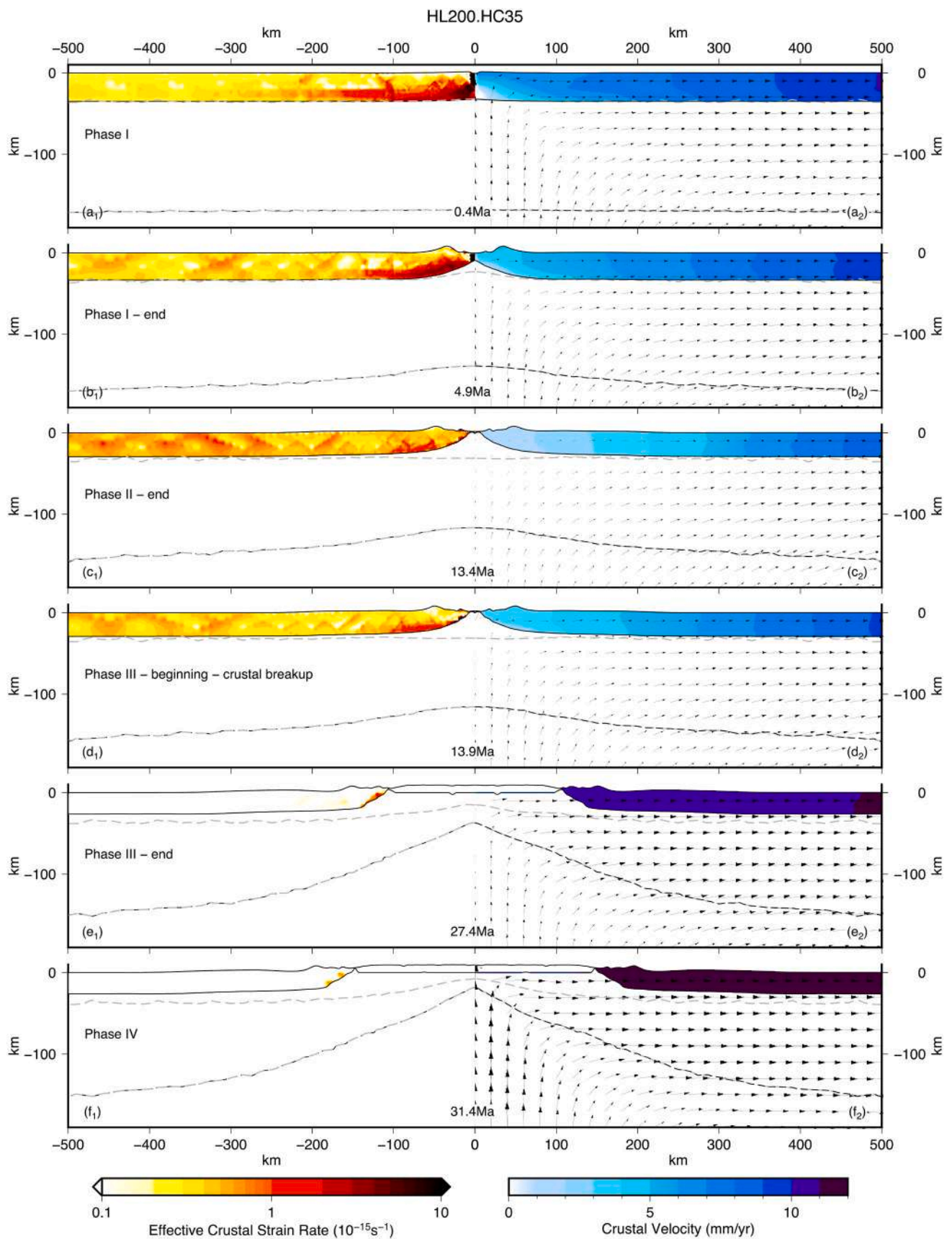
Fig. 4. Effective crustal strain rate (left side) and intensity of crustal horizontal velocity and velocity fields (right side) predicted by model HL150.HC40 at different times after the beginning of forced extension. Gray dashed lines correspond to the 800 K and 1500 K isotherms. Solid black lines represent the envelopes of crustal- and mantle-type markers.

Fig. 5. Effective crustal strain rate (left side) and intensity of crustal horizontal velocity and velocity fields (right side) predicted by model HL200.HC35 at different times after the beginning of forced extension. Gray dashed lines correspond to the 800 K and 1500 K isotherms. Solid black lines represent the envelopes of crustal- and mantle-type markers.
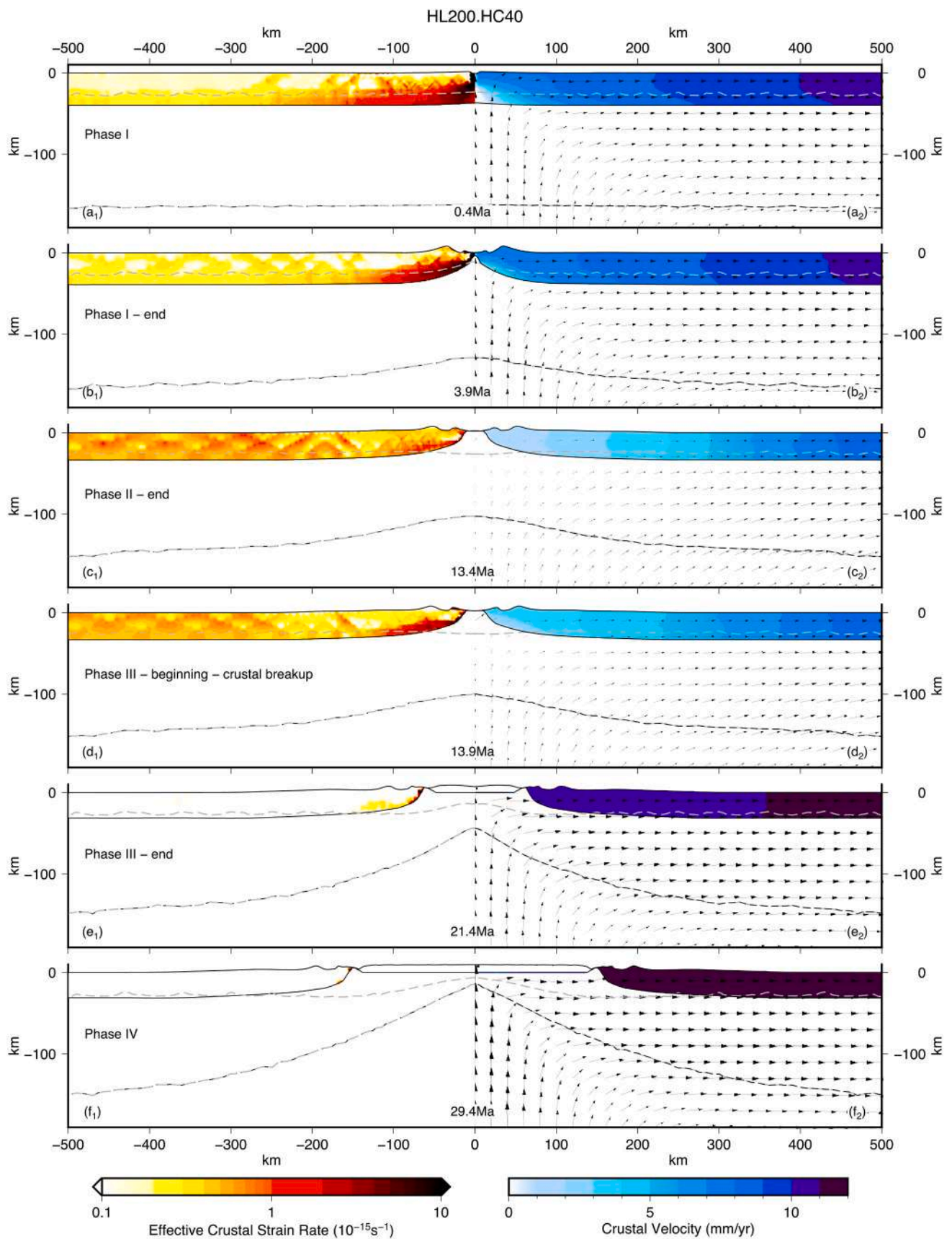
Fig. 6. Effective crustal strain rate (left side) and intensity of crustal horizontal velocity and velocity fields (right side) predicted by model HL200.HC40 at different times after the beginning of forced extension. Gray dashed lines correspond to the 800 K and 1500 K isotherms. Solid black lines represent the envelopes of crustal- and mantle-type markers.
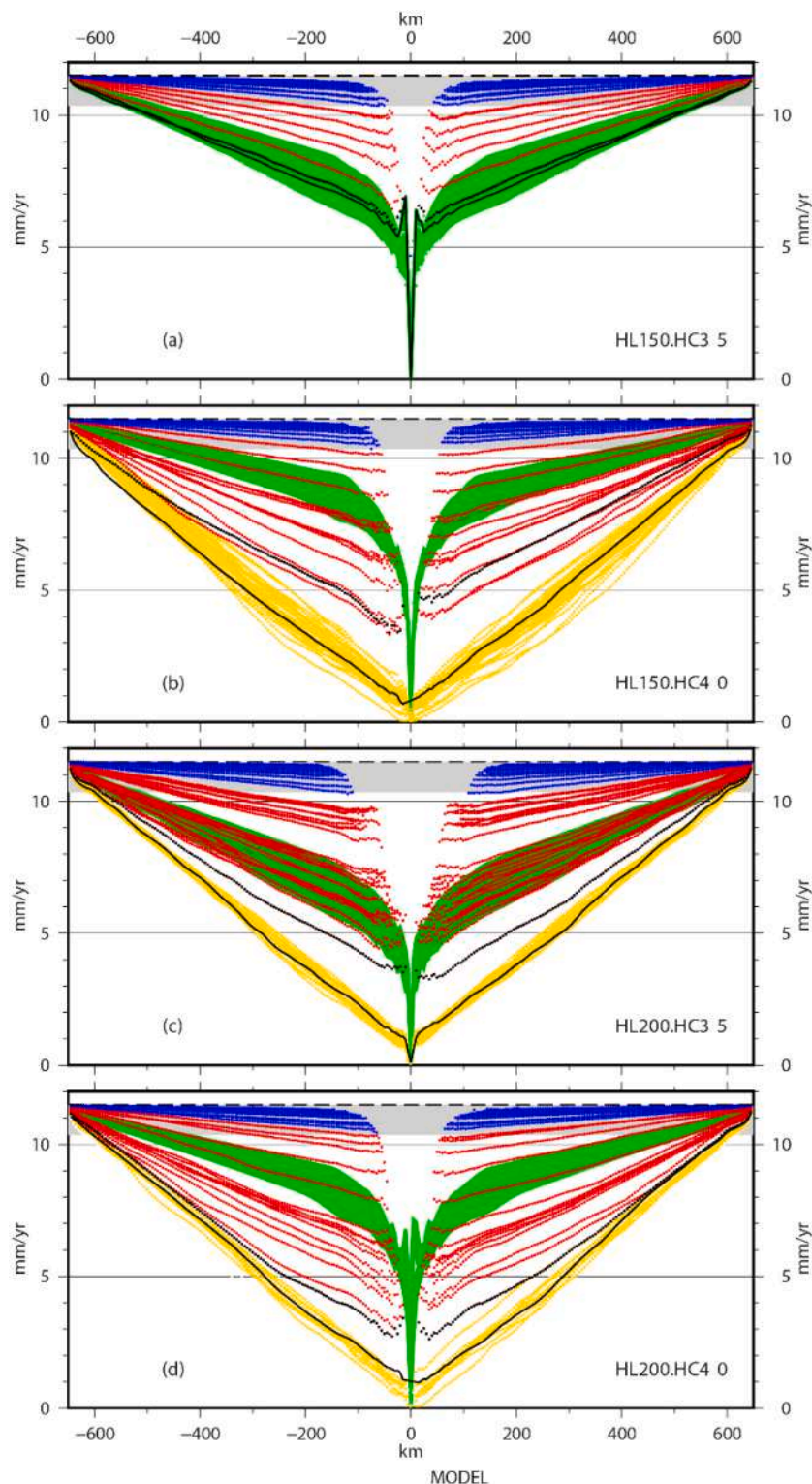
Fig. 7. Horizontal velocities vertically averaged on crustal thickness, predicted by models HL150.HC35 (a), HL150.HC40 (b), HL200.HC35 (c) and HL200.HC40 (d) at different distances from the ridge along the model during the different evolutionary phases (colors). The time step between lines is 0.5 Ma. Solid and dotted black lines indicate the average horizontal crustal velocity just before (end of phase II) and just after (beginning of phase III) crustal separation. Gray areas indicate the 10% tolerance in velocity used to define phase IV.

	HL150.HC35	HL150.HC40	HL200.HC35	HL200.HC40
PHASE 1	0Ma ÷ 5.9Ma	0Ma ÷ 2.9Ma	0Ma ÷ 4.9Ma	0Ma ÷ 3.9Ma
PHASE 2	----	3.4Ma ÷ 19.9Ma	5.4Ma ÷ 13.4Ma	4.4Ma ÷ 13.4Ma
PHASE 3	6.4Ma ÷ 9.4Ma	20.4Ma ÷ 26.4Ma	13.9Ma ÷ 27.4Ma	13.9Ma ÷ 21.4Ma
PHASE 4	9.9Ma ÷ 24.4Ma	26.9Ma ÷ 40.4Ma	27.9Ma ÷ 35.4Ma	21.9Ma ÷ 34.4Ma

crustal breakup occurs at the end of phase I (black solid lines in Fig. 7a).

After crustal breakup (beginning of phase III) the magnitude of the crustal horizontal velocity progressively increases in all models both in space (toward the passive margin) and in time with the progression of model evolution (panels d_2 of Figs. 3-6). These changes are compatible with the variation in time of the oceanic spreading rate. Consequently, the effective strain rate decreases over time until the crust starts moving

as a rigid block, with the same velocities as those imposed at the marginal sides of the model.

Fig. 7 shows that local horizontal contraction may occur at crustal level after crustal breakup, evident in terms of a value of the horizontal velocity that increases moving toward the axial zone. It could be correlated to the coeval intensification of the uprising mantle flow in the central part of the model, as evidenced by the arrows represented in
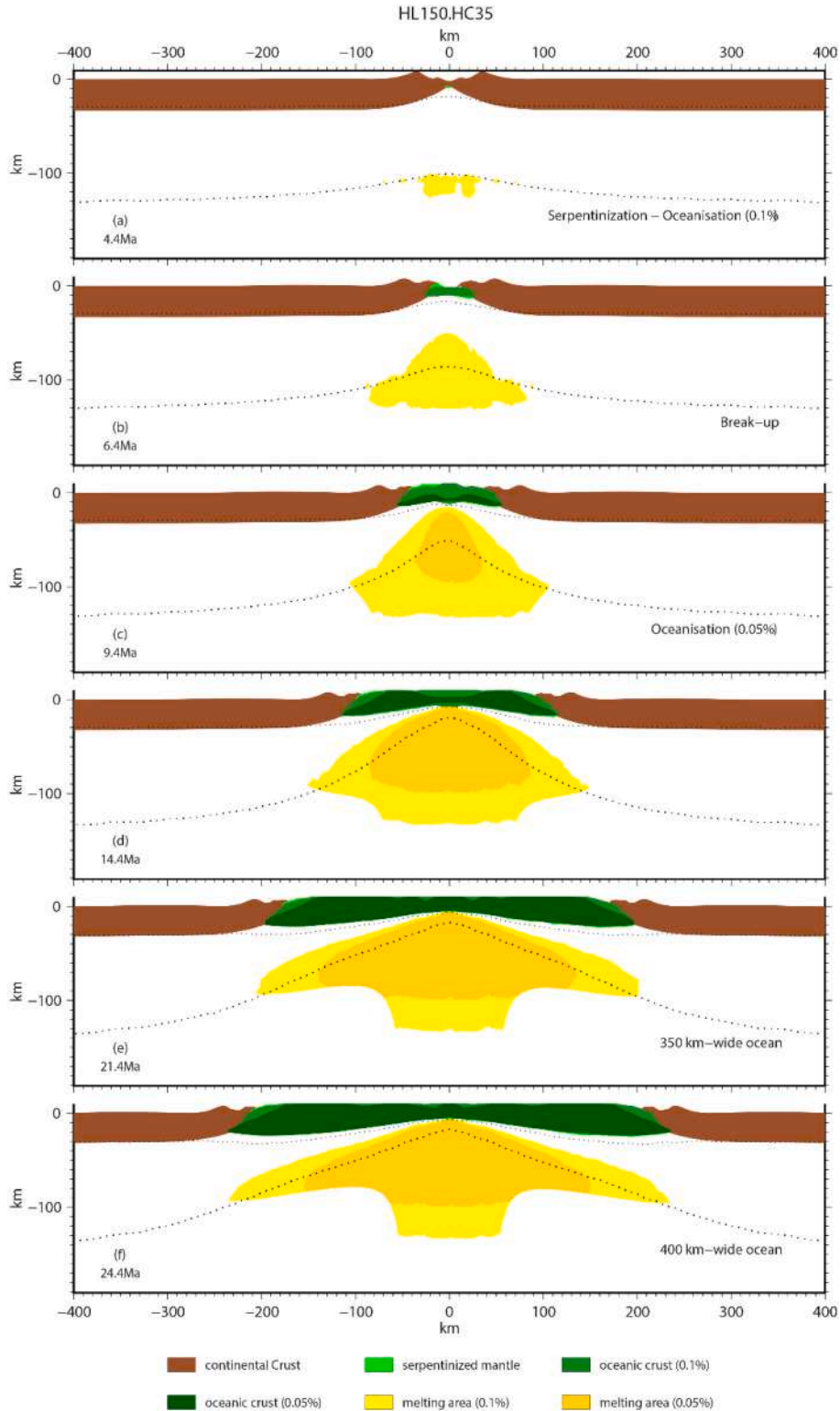

Fig. 8. Marker distributions predicted by model HL150.HC35 at different times from the beginning of forced extension. Different colors indicate different material types as specified in the legend. See text for more details. Black dotted lines correspond to the 800 K and 1500 K isotherms.

Figs. 3-6. A deeper investigation would be necessary to confirm this hypothesis but it is out of the scope of the present paper.

We assume that phase III ends when the crustal horizontal velocities differ by less than 10% from the maximum value prescribed at the marginal sides of the model (i.e., they are greater than 10.35 mm/year) and the effective strain rate is decreased anywhere well below $10^{-16}\,\text{s}^{-1}$, as shown in panels e Fig. 3 (HL150.HC35 model, at 9.4 Ma), 4 (HL150. HC40 model, at 26.4 Ma), 5 (HL200.HC35 model, at 27.4 Ma) and 6 (HL200.HC40 model, at 21.4 Ma). The sole exception occurs near the passive margin, where values of the effective strain rate higher than $10^{-15}\,\text{s}^{-1}$ are still induced at the Moho level by basal shear due to the rising mantle. Based on the definition given in Section 3, at the end of phase III lithospheric breakup is accomplished.

Finally, the last phase (IV) is characterized by two sections of crust that move as rigid blocks, with a velocity that, within a tolerance of 10%, is equal to that prescribed at the marginal sides. During this phase the extension of the central part of the model domain is driven by the upwelling mantle flow only and is accommodated by seafloor spreading (panel f of Figs. 3-6). As mentioned in Section 1, continental extension in the Gulf of Aden culminated in crustal rupture at approximately 16 Ma, and the accretion of new oceanic lithosphere in the central portion of the study area led to the formation of a 300 km-wide ocean. Our results agree with the analysis of the dragged samples along the mid-ocean ridge axis, as stated in Leroy et al., 2010 and Gass, 1970.

We stop the simulations when the two continental blocks are 400 km apart, which occurs at 24.4 Ma for model HL150.HC35, 40.4 Ma for model HL150.HC40, 35.4 Ma for model HL200.HC35 and 34.4 Ma for model HL200.HC40 (Figs. 3f, 4f, 5f and 6f, respectively). The long simulation time span also allows us to simulate the formation of the OCT zone, if this should develop.

4.2. Partial melting and oceanization

In all models, mantle serpentinization occurs during the early stages of evolution at the base of the thinned continental crust whose thickness is lower than 10 km in agreement with Pérez-Gussinyé and Reston (2001). In particular, 4.4 Ma after the beginning of forced extension, mantle serpentinization is observed below the ridge axis in models HL150.HC35 (Fig. 8a) and HL150.HC40 (Fig. 9b), at 5.4 Ma in model HL200.HC35 (Fig. 10a) and at 3.9 Ma in model HL200.HC40 (Fig. 11a). Mantle serpentinization causes a local decrease in the viscosity and consequently an increase in the local velocity.

Our results on the depth of the serpentinized zone with a thinned continental crust in magma-poor rifted margins are consistent with Pinto et al. (2015) who, from field work, obtain for proximal rift domains the possibility of highly extended (thinned) continental crust, lower than 10 km, which agrees with our modeling approach that does not contain faults or structural discontinuities, (Figs. 8a, 9b, 10a, 11a).

As already stated in Section 2.2, we assume that the oceanic crust forms after the beginning of mantle partial melting. Considering wet peridotite with a total amount of H_2O equal to 0.05%, pressure and temperature conditions at the base of the lithosphere are favorable for the formation of oceanic lithosphere after a relatively short time from crustal breakup for models HL150.HC35 (3 Ma, Fig. 8c) and HL150. HC40 (4 Ma, Fig. 9d). In contrast, for models HL200.HC35 and HL200. HC40, favorable pressure and temperature conditions are reached 10 Ma and 6.5 Ma after the occurrence of crustal breakup (Figs. 10d and 11d, respectively).

Considering wet peridotite with a total amount of H_2O equal to 0.1%, in models HL150.HC35 and HL150.HC40, favorable pressure and temperature conditions are reached 2 Ma and 17 Ma before the occurrence of crustal breakup (Figs. 8a and 9a, respectively). Similarly, in models HL200.HC35 and HL200.HC40, the formation of oceanic crust still starts after crustal breakup, namely, 4.5 and 2.5 Ma (Figs. 10c and 11c, respectively).

As stated in Section 3, for the formation of the OCT, partial melting must occur after mantle serpentinization and our results show that this condition is satisfied in all models considering wet peridotite with a total amount of H_2O equal to 0.05%. In this case, at the time when the two continents are separated by a distance of 400 km, the denuded serpentinized mantle covers an area of variable width, from approximately 30 km at both continental margins in model HL150.HC35 (light and medium green colour in Fig. 8f) to 50 km in model HL150.HC40 (Fig. 9f) and 70 km in model HL200.HC40 (Fig. 11f). In the HL200.HC35 model, the OCT zone lies below the oceanic crust; therefore, oceanization does not occur (Fig. 10f).

Considering peridotite with a total amount of H_2O equal to 0.1%, the conditions for OCT formation are predicted only by models HL200.HC35 and HL200.HC40, and OCT domain widths ranging from 80 km to 60 km develop (light green in Figs. 10f and 11f, respectively). In the case of 0.1% hydrated peridotite, models HL150.HC35 and HL150.HC40 predict partial melting before crustal breakup, thus preventing the development of an OCT.

Our model results indicate that partial melting can occur before breakup (panel a of Fig. 9), and the oceanic crust could underplate the lithosphere, in agreement with observation in continental rifts of the northernmost part of the Central Red Sea (Ligi et al., 2012).

Fig. 12 synthesizes the main stages of the deformation history predicted by the implemented models in terms of the timing of crustal breakup, serpentinization and melting with respect to the four thermomechanical phases. Our results show that a thicker lithosphere makes less important the variation in crustal thickness on the breakup timing which in fact is the same for the two models characterized by a 200 km thick lithosphere. The reduction of lithospheric thickness allows to emphasizes the effect of crustal variation on the crustal break up timing which occurs earlier for a thinner crust.

5. Discussion

In this study, we simulate the transition from continental rifting to oceanic spreading in the Gulf of Aden by means of a 2D numerical model based on the results of geodynamic studies and integrated modeling of elevation, geoid data and thermal analysis. A prescribed velocity of 11.5 mm/yr is applied at both sides of the domain to fit the present-day kinematics of the study area. Furthermore, we adopt initial thicknesses of 35 and 40 km for the continental crust and 150 and 200 km for the lithosphere.

A main result is that the thermomechanical evolution of the system can be separated into four phases with various durations for the different models:

a) phase I is characterized by horizontal crustal velocities that slowly decrease from the boundary of the model to approximately 100 km from the ridge and by rapid decreases in velocities in the central portion of the domain; as a consequence, low strain rates characterize the crust away from the ridge, while very high strain rates characterize the surroundings of the future ridge, as also shown in the modeled strain rate pattern in Brune and Autin (2013), Brune (2014) and Schettino et al. (2019);

b) phase II has a crust characterized by velocities that are almost constant in time but decrease linearly in space from the lateral sides to the future ridge. During this phase, the highest velocity gradients and strain rates are observed (e.g., Brune and Autin, 2013; Watremez et al., 2013; Brune, 2014;). Phase II ends when continental crustal breakup occurs after 19.9 Ma from the beginning of rifting in model HL150.HC40 and after 13.4 Ma in models HL200.HC35 and HL200. HC40. This phase is not recorded by model HL150.HC35, which exhibits crustal breakup after 5.9 Ma, i.e., at the end of phase I;

c) phase III characterizes the post crustal breakup evolution in all models. During this phase, there are fast increases in both horizontal velocities in the crust and vertical velocities corresponding to the ridge. Compared to phase II, the lateral velocity gradients are less
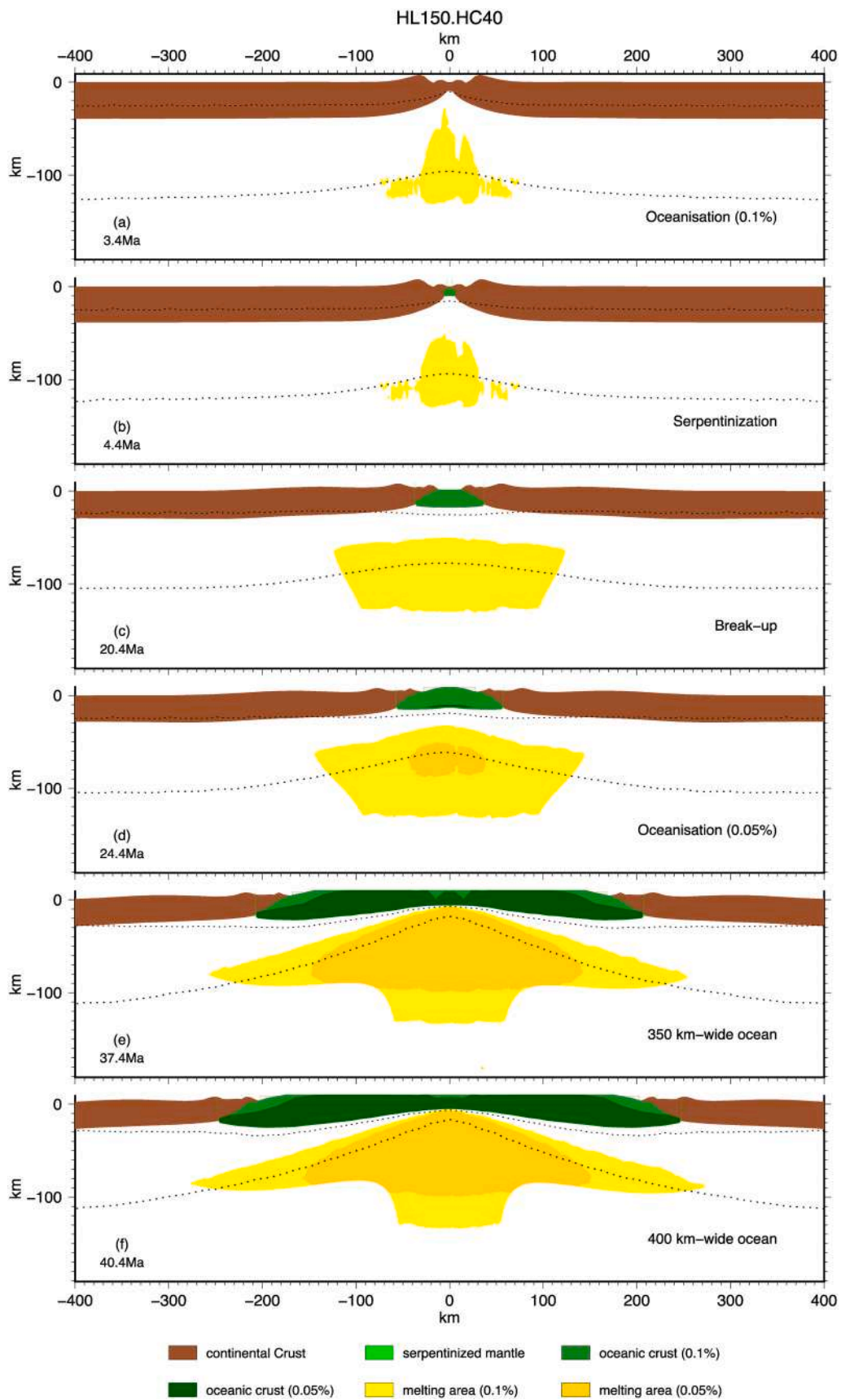
Fig. 9. Marker distributions predicted by model HL150.HC40 at different times from the beginning of forced extension. Different colors indicate different material types as specified in the legend. See text for more details. Black dotted lines correspond to the 800 K and 1500 K isotherms.
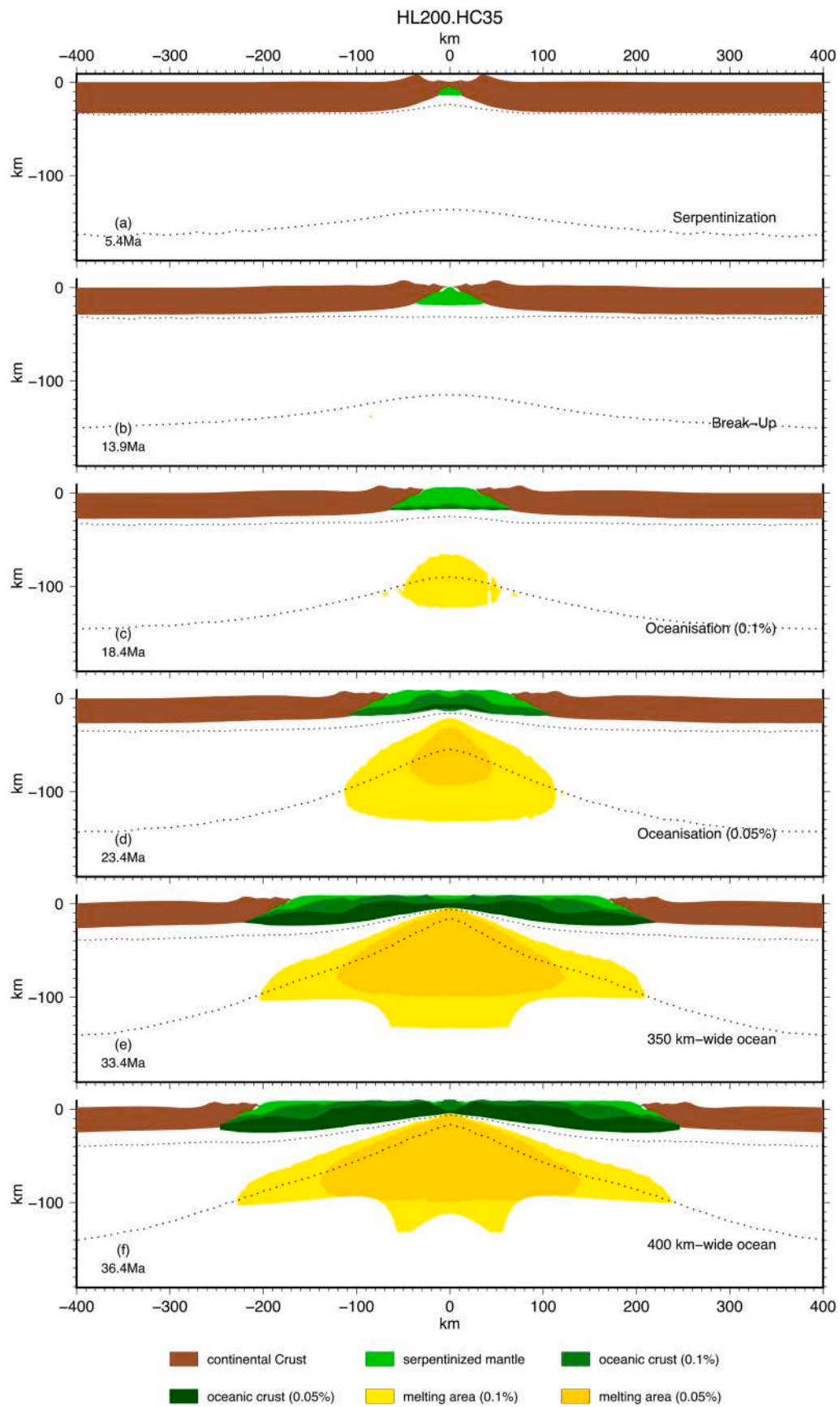
Fig. 10. Marker distributions predicted by model HL200.HC35 at different times from the beginning of forced extension. Different colors indicate different material types as specified in the legend. See text for more details. Black dotted lines correspond to the 800 K and 1500 K isotherms.
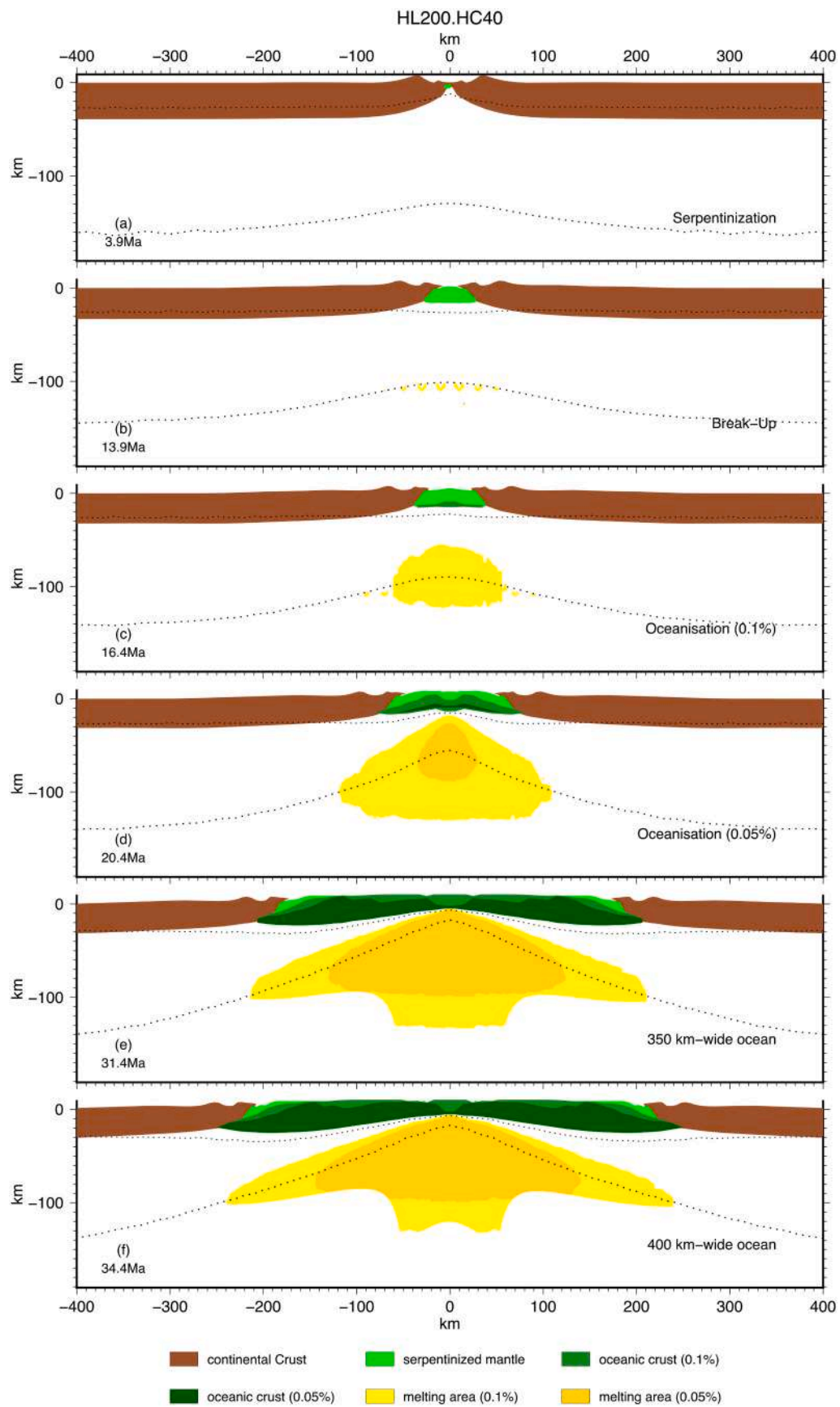
HL200.HC40

Fig. 11. Marker distributions predicted by model HL200.HC40 at different times from the beginning of forced extension. Different colors indicate different material types as specified in the legend. See text for more details. Black dotted lines correspond to the 800 K and 1500 K isotherms.
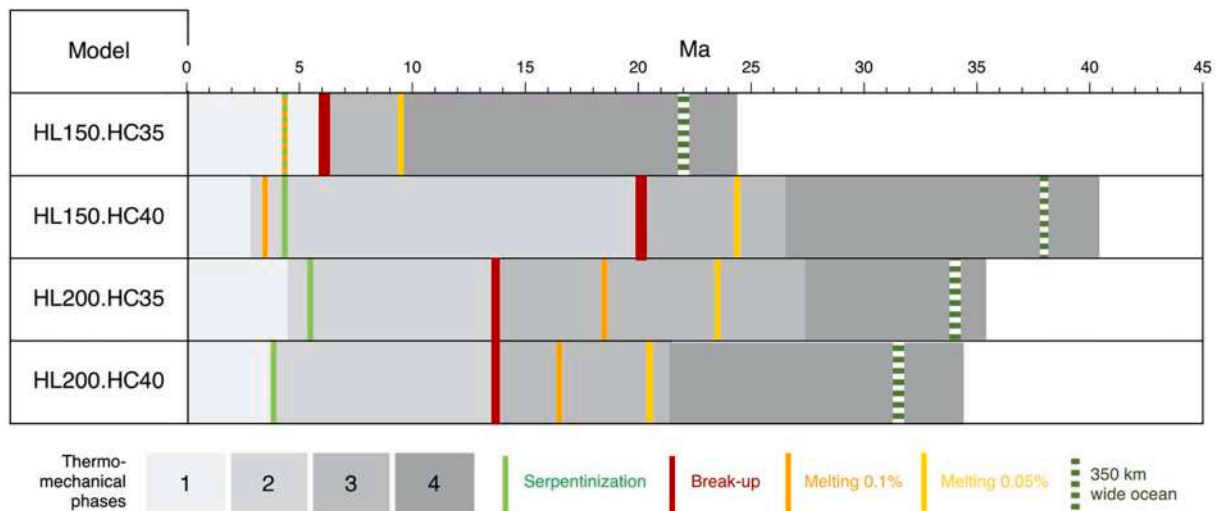
Fig. 12. Synthetic representation of the main stages of the deformation history predicted by the models implemented in this study.

intense and even decrease over time, resulting in strain rates that are lower than those predicted for phase II. This phase lasts 3 Ma for model HL150.HC35, 6 Ma for models HL150.HC40, 13.5 Ma for model HL200.HC35 and 7.5 Ma for HL200.HC40. At the end of phase III, when the lithospheric breakup occurs, the horizontal velocities in the crustal blocks are constant, with values higher than 10 mm/yr in all models, and strain rates are very low (well below 10^{-16} s^{-1}) compared to those predicted during previous phases;

d) phase IV is marked by two sections of crust that move as rigid blocks with a velocity that, within a tolerance of 10%, is equal to that prescribed at the marginal sides, comparable with the velocity trend shown in Marotta et al. (2018). This phase ends when the two continental blocks are 400 km apart, that is after 24.4, 40.4, 35.4 and 34.4 Ma from the beginning of evolution, for models HL150.HC35, HL150.HC40, HL200.HC35 and HL200.HC40, respectively.

The Gulf of Aden is characterized by different velocities of oceanic spreading, which increase from west to east. In particular, west of the SSFZ, where magnetic anomalies date the formation of the oceanic floor at 2–3 Ma (Bellahsen et al., 2003; Bellahsen et al., 2006; Fournier et al., 2010; Leroy et al., 2010; Bonatti et al., 2015), velocities are approximately 13 mm/yr, while in the east, in proximity to the AFFZ, where magnetic anomalies date the formation of the oceanic floor at 16–17 Ma (Bellahsen et al., 2003; Bellahsen et al., 2006; Fournier et al., 2010; Leroy et al., 2010; Bonatti et al., 2015), velocities are approximately 20 mm/yr. The variation velocities predicted near the passive margin at different times of the evolution may contribute to explain the different velocities observed in the Gulf of Aden along different transects characterized by different ages of spreading. In fact, models HL150.HC40, HL200.HC35 and HL200.HC40 predict a total spreading rate of 12–13 mm/yr 3 Ma after the breakup at approximately 100 km from the ridge, which is compatible with the velocity observed at present in proximity to the SSFZ; the sole exception occurs for model HL150.HC35. Furthermore, all models predict a total spreading rate of 21–22 mm/yr 15–16 Ma after the breakup, at approximately 150 km from the ridge, as observed at present in proximity to the AFFZ.

Our results show that mantle serpentinization does not depend strictly on the initial thickness of crust and lithosphere: for almost all models it starts at 4.4 Ma after the beginning of rifting and only in model HL200.HC35 serpentinization occurs one million years later. In contrast, the timing of mantle partial melting strongly depends on the thickness and thus on the initial thermal state of the lithosphere (Mckenzie and Bickle, 1988; Schmeling, 2000; Furlong and Chapman, 2013) (compare Figs. 8 and 9 and Figs. 10 and 11). In particular, considering wet

peridotite with a total amount of H$_2$O equal to 0.1%, partial melting occurs very early for models with thinner lithosphere (Figs. 8a and 9a, for models HL150.HC35 and HL150.HC40, respectively) and even before the occurrence of serpentinization when a thicker initial crust is considered (model HL150.HC40). This result is caused by the higher thermal conditions of thinner lithosphere (models HL150.HC35 and HL150.HC40) and, in the same way, by the thicker continental crust of model HL150.HC40, which generates higher temperatures at the Moho level due to the higher production of radiogenic energy. Since the initial thermal conditions of the thin models are not very different from those required for melting in 0.1% hydrated mantle, mantle melting occurs very quickly in these models. In contrast, in colder models, a long time is required to increase the thermal state to pressure–temperature conditions that are suitable for mantle melting.

When peridotite with a total amount of H$_2$O equal to 0.05% is assumed, mantle partial melting needs a higher thermal state (temperatures approximately 100 °C higher than those required for hydrated mantle with 0.1% water content). Consequently, models take more time to reach melting for 0.05% hydrated mantle. For all models, melting of 0.05% hydrated mantle occurs after breakup and 4 to 5 Ma after melting of 0.1% hydrated mantle. The sole exception occurs for model HL150.HC40, which predicts melting of 0.05% hydrated mantle only 20 Ma later than that of wetter mantle. The highest temperatures and the lowest stiffness characterizing this model make the stress transmission less effective, and the localization of thinning that drives the local increase in temperature occurs very late.

As mentioned in Section 1, the Gulf of Aden is a juvenile ocean that began rifting during the late Eocene between 42 and 35 Ma (Watchorn et al., 1998; Basuyau et al., 2010; Leroy et al., 2010). Magnetic data indicate that the emplacement of the oceanic floor can be dated at 19.7 Ma in the easternmost part of the Sheba Ridge, at 17.6 Ma up to the AFFZ and at approximately 16 Ma between the AFFZ and the SSFZ (Bellahsen et al., 2003; Bellahsen et al., 2006; Fournier et al., 2010; Leroy et al., 2010; Bonatti et al., 2015). These results suggest a period of 20 Ma characterized by extensional tectonics before the occurrence of continental breakup, and subsequently an oceanic/OCT domain forms, with width from approximately 350–400 km in proximity to the Sheba Ridge, where the opening rate is 23 mm/yr, to approximately 200 km near the SSFZ, where the opening rate is 16 mm/yr.

West of the SSFZ (Fig. 1), which marks the limit of the Afar plume influence, the Gulf of Aden exhibits volcanic margins without the formation of an OCT; partial melting possibly occurs before crustal breakup, and oceanic crust is created as soon as the continental crust is broken apart by dikes (Watremez et al., 2013). East of the SSFZ, the Gulf

is characterized by magma-poor rifted margins where partial melting occurs after crustal breakup, and a narrow OCT (15–50 km) forms between the last continental crust and the first oceanic crust (Bauer et al., 2000; Watremez et al., 2003), which presents strong along-margin variations with serpentinization and little volcanism (Watremez et al., 2013). In particular, in the eastern part, oceanic crust begins to form approximately 1 Ma after continental breakup, with the consequent formation of an approximately 25–40 km-wide OCT (Nonn et al., 2019).

The comparison between numerical models and the natural Gulf of Aden mainly focuses on the central sector of the Gulf between the SSFZ and the AFFZ, where the emplacement of the oceanic floor was a continuous process (Fournier et al., 2010). Therefore, considering an extensional period lasting 20 Ma before the breakup, the HL150.HC35 model is not compatible with the geodynamic reconstructions because of its early breakup, which is predicted to occur approximately 7 Ma after the beginning of forced extension (Fig. 7a). In addition, model HL150. HC35, when a percentage of H_2O equal to 0.1% is accounted for in the mantle, predicts mantle serpentinization that is coeval with mantle partial melting, thus not satisfying the conditions for OCT formation (Fig. 8a). Similarly, models characterized by a 200 km-thick lithosphere predict breakup approximately 14 Ma after the start of rifting (Fig. 7c-d). Further, considering peridotite with a total amount of H_2O equal to 0.05%, models HL200.HC35 and HL200.HC40 show delays between crustal breakup and mantle melting ranging from 6.5 to 10 Ma (Figs. 8d and 9d), with the development of an OCT larger than that observed in the Gulf of Aden.

Considering 0.05% hydrated mantle, model HL150.HC40 is the most appropriate to reproduce the geodynamic evolution of the study area; this model is also in agreement with crustal and lithospheric thicknesses based on geoid data and thermal analysis (Globig et al., 2016) that show a thinned continental crust (passive margin), an OCT zone and an oceanic lithosphere, which characterize the final structure of the system. In fact, model HL150.HC40 predicts the onset of mantle serpentinization under the continental crust before the occurrence of mantle partial melting (Fig. 9a), which occurs 4 Ma after crustal breakup. This sequence of events allows the formation of an approximately 40–50 km-wide OCT (Fig. 9f). In addition, the oceanic domain in this model reaches an extension of 350–400 km by 37–40 Ma after the beginning of forced extension, in agreement with the ages of the first extensional structures observed in the area.

The westernmost part of the area, near the SSFZ, is characterized by a transition between magma-rich and magma-poor margins, moving from west to east (Fig. 1) and by the absence of an OCT. Therefore, models that predict dynamics compatible with the evolution of the margins of this area are models HL150.HC35 and HL150.HC40 with 0.1% hydrated mantle because mantle serpentinization occurs synchronously with mantle partial melting and the OCT does not form. However, model HL150.HC35 does not show a timing compatible with the geodynamic reconstruction of the area, as revealed previously. In addition, model HL150.HC40 fits the westernmost part of the area characterized by volcanic margins since melting occurs before continental breakup. Geochemical studies of MORB that incorporate a component from a plume-associated source suggest H_2O concentrations in plume sources ranging from 0.03 to 0.1% (300–1000 ppm; Hirschmann, 2006), compatible with the peridotite water content used in our simulations.

Our results show that model HL150.HC40 describes the evolution of the central sector of the Gulf of Aden well, and the variations in the features along the passive margins could be related to lateral variations in the amount of H_2O in the mantle, which determine different times of mantle melting. In fact, melting in the case of 0.05% hydrated mantle leads to the formation of a magma-poor margin and a narrow OCT, while increasing the water content up to 0.1% causes melting to occur before continental breakup, with a consequent volcanic margin and the absence of an OCT. The increase in mantle water storage can be associated with the presence of the Afar plume in the westernmost portion of the Gulf of Aden; a similar situation is also observed in proximity to a

mantle plume along the Reykjanes Ridge in the North Atlantic (Nichols et al., 2002).

The dependence of mantle hydration on mantle melting and of the timing of breakup on the thickness of the crust and lithosphere, allow us to further constrain the latter compared with previous analyses. In particular, our results define an upper bound for crustal thickness of 40 km, in agreement with the findings obtained from the integration of elevation and geoid data and thermal analysis of north Africa by Globig et al. (2016).

Our results for model characterized by 150 km -thick lithosphere show melting production before continental breakup, in agreement with numerical models by Pérez-Gussinyé et al. (2006) accounting for an extensional velocity of 1 cm/yr.

6. Conclusion

We developed 2D thermomechanical numerical models of passive rifting to investigate the evolution of the lithosphere in the Gulf of Aden. The models are founded on integrated modeling of elevation, geoid data and thermal analysis and account for the present-day kinematics observed between the Arabian plate and Africa (Nubia) and Somalia.

For the combination of parameters assumed in the present analysis, our results indicate that, in addition to support a deformation history that develops in 4 different phases, the timing of mantle serpentinization is not affected by the initial thermal configuration of the system, and mantle serpentinization starts a few million years (4–5 Ma) after the onset of rifting for all models, well before crustal breakup.

Furthermore, our results show that the OCT always develops when the rifting to oceanization transition occurs in case of a thick lithosphere. In contrast, with a thin lithosphere, wet peridotite with a total amount of H_2O equal to 0.05% is required to drive the development of an OCT zone. Model predictions, in terms of the times of different deformation phases and sizes of the oceanic domain and the OCT zone, are compared with information based on magnetic data analysis and on the observed distribution of volcanic margins in the region between the SSFZ and the AFFZ, where emplacement of the oceanic floor was a continuous process. Model results confirm that the model with an initial 150 km-thick lithosphere and a 40 km-thick crust is the most appropriate to reproduce the geodynamic evolution of the study area when 0.05% hydrated mantle is considered. This model is also in agreement with the crust and lithosphere thicknesses based on thermal analysis and geoid data, which imply that the central part of the Gulf of Aden started to rift at approximately 37–40 Ma in its easternmost sector and is characterized by the sequence of a thinned passive margin, an OCT zone and an oceanic domain.

The best-fit model predicts a 40–50 km-wide OCT zone and a 350–400 km-wide oceanic domain in the eastern sector, while a 100 km-wide oceanic domain with no OCT zone is predicted in the western sector of the Gulf of Aden. The variations in features along the passive margins from west to east are ascribable to lateral variations in the amount of H_2O in the mantle, which determines the different times of mantle melting. In particular, an increase from 0.05% to 0.1% hydrated mantle associated with the Afar plume might have preceded mantle melting and thus precluded the development of an OCT zone in the western sector of the Gulf of Aden. Our approach allows us to obtain a robust estimate of the crustal thickness of 40 km, thus definitively choosing the upper bound in previous estimates of this parameter for the crust surrounding the Gulf of Aden.

Credit author statement

All the authors contributed equally to: Conceptualization, Writing the original draft, review and editing.

Arcangela Bollino, Anna Maria Marotta, Alessandro Regorda Contributed equally to: Methodology, Software, Validation and Visualization.

References

ArRajehi, A., McClusky, S., Reilinger, R., Daoud, M., Alchalbi, A., Ergintav, S., Gomez, F., Sholan, J., Bou-Rabee, F., Ogubazghi, G., Haileab, B., Fisseha, S., Asfaw, L., Mahmoud, S., Rayan, A., Bendik, R., Kogan, L., 2010. Geodetic constraints on present-day motion of the Arabian Plate: implications for Red Sea and Gulf of Aden rifting. Tectonics 29 (3). https://doi.org/10.1029/2009TC002482.

Autin, J., Leroy, S., Beslier, M.-O., Acremont, E., Razin, P., Ribodetti, A., Bellahsen, N., Robin, C., Al Toubi, K., 2010. Continental break-up history of a deep magma-poor margin based on seismic reflection data (northeastern Gulf of Aden margin, offshore Oman). Geophys. J. Int. 180 (2), 501–519. https://doi.org/10.1111/j.1365-246X.2009.04424.x.

Autin, J., Bellahsen, N., Leroy, S., Husson, L., Beslier, M.O., d'Acremont, E., 2013. The role of structural inheritance in oblique rifting: Insights from analogue models and application to the Gulf of Aden. Tectonophysics 607, 51–64. https://doi.org/10.1016/j.tecto.2013.05.041.

Basuyau, C., Tiberi, C., Leroy, S., Stuart, G., Al-Lazki, A., Al-Toubi, K., Ebinger, C., 2010. Evidence of partial melting beneath a continental margin: case of Dhofar, in the Northeast Gulf of Aden (Sultanate of Oman). Geophys. J. Int. 180 (2), 520–534. https://doi.org/10.1111/j.1365-246X.2009.04438.x.

Bauer, K., Neben, S., Schreckenberger, B., Emmermann, R., Hinz, K., Fechner, N., Gohl, K., Schulze, A., Trumbull, R.B., Weber, K., 2000. Deep structure of the Namibia continental margin as derived from integrated geophysical studies. J. Geophys. Res. Solid Earth 105 (B11), 25829–25853. https://doi.org/10.1029/2000JB900227.

Bellahsen, N., Faccenna, C., Funiciello, F., Daniel, J.M., Jolivet, L., 2003. Why did Arabia separate from Africa? Insights from 3-D laboratory experiments. Earth Planet. Sci. Lett. 216 (3), 365–381. https://doi.org/10.1016/S0012-821X(03)00516-8.

Bellahsen, N., Fournier, M., d'Acremont, E., Leroy, S., Daniel, J.M., 2006. Fault reactivation and rift localization: Northeastern Gulf of Aden margin. Tectonics 25 (1). https://doi.org/10.1029/2004TC001626.

Beucher, R., Huismans, R.S., 2020. Morphotectonic evolution of passive margins undergoing active surface processes: large-scale experiments using numerical models. Geochem. Geophys. Geosyst. 21 (5), e2019GC008884 https://doi.org/10.1029/2019GC008884.

Bonatti, E., Cipriani, A., Lupi, L., 2015. The Red Sea: birth of an ocean. In: The Red Sea. Springer, Berlin, Heidelberg, pp. 29–44.

Bosworth, W., 2015. Geological evolution of the Red Sea: Historical background, review, and synthesis. In: The Red Sea. Springer, Berlin, Heidelberg, pp. 45–78.

Bosworth, W., Huchon, P., McClay, K., 2005. The red sea and gulf of Aden basins. J. Afr. Earth Sci. 43 (1–3), 334–378. https://doi.org/10.1016/j.jafrearsci.2005.07.020.

Brune, S., 2014. Evolution of stress and fault patterns in oblique rift systems: 3-D numerical lithospheric-scale experiments from rift to breakup. Geochem. Geophys. Geosyst. 15 (8), 3392–3415.

Brune, S., Autin, J., 2013. The rift to break-up evolution of the Gulf of Aden: insights from 3D numerical lithospheric-scale modelling. Tectonophysics 607, 65–79. https://doi.org/10.1016/j.tecto.2013.06.029.

Chenin, P., Schmalholz, S.M., Manatschal, G., Karner, G.D., 2018. Necking of the lithosphere: a reappraisal of basic concepts with thermo-mechanical numerical modeling. J. Geophys. Res. Solid Earth 123 (6), 5279–5299. https://doi.org/10.1029/2017JB014155.

Christensen, U.R., 1992. An Eulerian technique for thermomechanical modeling of lithospheric extension. J. Geophys. Res. Solid Earth 97 (B2), 2015–2036.

Clague, D.A., 1987. Hawaiian xenolith populations, magma supply rates, and development of magma chambers. Bull. Volcanol. 49 (4), 577–587. https://doi.org/10.1007/BF01079963.

Crameri, F., Schmeling, H., Golabek, G.J., Duretz, T., Orendt, R., Buiter, S.J.H., May, D. A., Kaus, B.J.P., Gerya, T.V., Tackley, P.J., 2012. A comparison of numerical surface topography calculations in geodynamic modelling: an evaluation of the 'sticky air'method. Geophys. J. Int. 189 (1), 38–54. https://doi.org/10.1111/j.1365-246X.2012.05388.x.

Dixon, J.E., Leist, L., Langmuir, C., Schilling, J.G., 2002. Recycled dehydrated lithosphere observed in plume-influenced mid-ocean-ridge basalt. Nature 420 (6914), 385–389. https://doi.org/10.1038/nature01215.

Donea, J., Huerta, A., 2003. Finite Element Methods for Flow Problems. John Wiley & Sons.

Farangitakis, G.P., Heron, P.J., McCaffrey, K.J.W., van Hunen, J., Kalnins, L.M., 2020. The impact of oblique inheritance and changes in relative plate motion on the development of rift-transform systems. Earth Planet. Sci. Lett. 541, 116277 https://doi.org/10.1016/j.epsl.2020.116277.

Fournier, M., et al., 2010. Arabia–Somalia plate kinematics, evolution of the Aden–Owen–Carlsberg triple junction, and opening of the Gulf of Aden. J. Geophys. Res. 115 (B4) https://doi.org/10.1029/2008JB006257 (n/a–n/a).

Furlong, K.P., Chapman, D.S., 2013. Heat flow, heat generation, and the thermal state of the lithosphere. Annu. Rev. Earth Planet. Sci. 41, 385–410.

Gass, I.G., 1970. The evolution of volcanism in the junction area of the Red Sea, Gulf of Aden and Ethiopian rifts. Philos. Trans. R. Soc. Lond. A.267, 369–381.

Gerya, T.V., 2013. Three-dimensional thermomechanical modeling of oceanic spreading initiation and evolution. Phys. Earth Planet. Inter. 214, 35–52. https://doi.org/10.1016/j.pepi.2012.10.007.

Gerya, T.V., Yuen, D.A., 2003. Rayleigh–Taylor instabilities from hydration and melting propel 'cold plumes' at subduction zones. Earth Planet. Sci. Lett. 212 (1–2), 47–62. https://doi.org/10.1016/S0012-821X(03)00265-6.

Globig, J., Fernàndez, M., Torne, M., Vergés, J., Robert, A., Faccenna, C., 2016. New insights into the crust and lithospheric mantle structure of Africa from elevation, geoid, and thermal analysis. J. Geophys. Res. Solid Earth 121 (7), 5389–5424. https://doi.org/10.1002/2016JB012972.

Gueydan, F., Morency, C., Brun, J.P., 2008. Continental rifting as a function of lithosphere mantle strength. Tectonophysics 460 (1–4), 83–93. https://doi.org/10.1016/j.tecto.2008.08.012.

Gulcher, A.J.P., Beaussier, S.J., Gerya, T.V., 2019. On the formation of oceanic detachment faults and their influence on intra-oceanic subduction initiation: 3D thermomechanical modeling. Earth Planet. Sci. Lett. 506, 195–208. https://doi.org/10.1016/j.epsl.2018.10.042.

Hansen, S.E., Rodgers, A.J., Schwartz, S.Y., Al-Amri, A.M., 2007. Imaging ruptured lithosphere beneath the Red Sea and Arabian Peninsula. Earth Planet. Sci. Lett. 259 (3–4), 256–265. https://doi.org/10.1016/j.epsl.2007.04.035.

Hirschmann, M.M., 2006. Water, melting, and the deep Earth H2O cycle. Annu. Rev. Earth Planet. Sci. 34, 629–653. https://doi.org/10.1146/annurev.earth.34.031405.125211.

Huchon, P., Khanbari, K., 2003. Rotation of the syn-rift stress field of the northern Gulf of Aden margin, Yemen. Tectonophysics 364 (3–4), 147–166. https://doi.org/10.1016/S0040-1951(03)00056-8.

Hughes, T.J.R., Liu, W., Brooks, J., 1979. Finite element analysis of incompressible viscous flows by the penalty function formulation. J. Comput. Phys. 30 (1), 1–60. https://doi.org/10.1016/0021-9991(79)90086-X.

Huismans, R.S., Beaumont, C., 2002. Asymmetric lithospheric extension: the role of frictional plastic strain softening inferred from numerical experiments. Geology 30 (3), 211–214.

Huismans, R.S., Beaumont, C., 2003. Symmetric and asymmetric lithospheric extension: Relative effects of frictional-plastic and viscous strain softening. J. Geophys. Res. Solid Earth 108 (B10).

Jourdon, A., Le Pourhiet, L., Mouthereau, F., May, D., 2020. Modes of propagation of continental breakup and associated oblique rift structures. J. Geophys. Res. Solid Earth 125 (9), e2020JB019906.

Katz, R.F., Spiegelman, M., Langmuir, C.H., 2003. A new parameterization of hydrous mantle melting. Geochemistry,Geophysics,Geosystems 4 (9). https://doi.org/10.1029/2002GC000433.

Larsen, H.C., Mohn, G., Nirrengarten, M., Sun, Z., Stock, J., Jian, Z., Zhong, L., 2018. Rapid transition from continental breakup to igneous oceanic crust in the South China Sea. Nat. Geosci. 11 (10), 782–789.

Leroy, S., d'Acremont, E., Tiberi, C., Basuyau, C., Autin, J., Lucazeau, F., Sloan, H., 2010. Recent off-axis volcanism in the eastern Gulf of Aden: implications for plume–ridge interaction. Earth Planet. Sci. Lett. 293 (1–2), 140–153. https://doi.org/10.1016/j.epsl.2010.02.036.

Leroy, et al., 2012. From rifting to oceanic spreading in the Gulf of Aden: a synthesis. Arab. J. Geosci. 5 (5), 859–901. https://doi.org/10.1007/s12517-011-0475-4.

Liao, J., Gerya, T., 2015. From continental rifting to seafloor spreading: insight from 3D thermo-mechanical modeling. Gondwana Res. 28 (4), 1329–1343.

Marotta, A.M., Spelta, E., Rizzetto, C., 2006. Gravity signature of crustal subduction inferred from numerical modelling. Geophys. J. Int. 166 (2), 923–938. https://doi.org/10.1111/j.1365-246X.2006.03058.x.

Marotta, A.M., Spalla, M.I., Gosso, G., 2009. Upper and lower crustal evolution during lithospheric extension: numerical modelling and natural footprints from the European Alps. Geol. Soc. Lond., Spec. Publ. 321 (1), 33–72.

Marotta, A.M., Roda, M., Conte, K., Spalla, M.I., 2018. Thermo-mechanical numerical model of the transition from continental rifting to oceanic spreading: the case study of the Alpine Tethys. Geol. Mag. 155 (2), 250–279. https://doi.org/10.1017/S0016756816000856.

Ligi, M., Bonatti, E., Bortoluzzi, G., Cipriani, A., Cocchi, L., Caratori Tontini, F., Carminati, E., Ottolini, L., Schettino, A., 2012. Birth of an ocean in the Red Sea: Initial pangs. Geochem. Geophys. Geosystems. https://doi.org/10.1029/2012GC004155.

Marotta, A.M., Restelli, F., Bollino, A., Regorda, A., Sabadini, R., 2020. The static and time-dependent signature of ocean–continent and ocean–ocean subduction: the case studies of Sumatra and Mariana complexes. Geophys. J. Int. 221 (2), 788–825.

Mckenzie, D.A.N., Bickle, M.J., 1988. The volume and composition of melt generated by extension of the lithosphere. J. Petrol. 29 (3), 625–679.

Nichols, A.R.L., Carrol, M.R., Hoskuldsson, A., 2002. Is the Iceland hot spot also wet? Evidence from the water contents of undegassed submarine and subglacial pillow basalts. Earth Planet. Sci. Lett. 202 (1), 77–87. https://doi.org/10.1016/S0012-821X (02)00758-6.

Nikolaeva, K., Gerya, T.V., Connolly, J.A., 2008. Numerical modelling of crustal growth in intraoceanic volcanic arcs. Phys. Earth Planet. Inter. 171 (1–4), 336–356.

Nonn, C., Leroy, S., Lescanne, M., Castilla, R., 2019. Central Gulf of Aden conjugate margins (Yemen-Somalia): Tectono-sedimentary and magmatism evolution in hybrid-type margins. Mar. Pet. Geol. 105, 100–123. https://doi.org/10.1016/j.marpetgeo.2018.11.053.

Pérez-Gussinyé, M., Reston, T.J., 2001. Rheological evolution during extension at nonvolcanic rifted margins: Onset of serpentinization and development of detachments leading to continental breakup. J. Geophys. Res. Solid Earth 106 (B3), 3961–3975.

Pérez-Gussinyé, M., Morgan, J.P., Reston, T.J., Ranero, C.R., 2006. The rift to drift transition at non-volcanic margins: Insights from numerical modelling. Earth Planet. Sci. Lett. 244 (1–2), 458–473. https://doi.org/10.1016/j.epsl.2006.01.059.

Petrunin, A.G., Kaban, M.K., El Khrepy, S., Al-Arifi, N., 2020. Mantle convection patterns reveal the mechanism of the Red Sea rifting. Tectonics 39 (2), e2019TC005829. https://doi.org/10.1029/2019TC005829.

Pinto, V.H.G., Manatschal, G., Karpoff, A.M., Viana, A., 2015. Tracing mantle-reacted fluids in magma-poor rifted margins: the example of A lpine T ethyan rifted margins. Geochem. Geophys. Geosyst. 16 (9), 3271–3308.

Rasul, N.M., Stewart, I.C., Nawab, Z.A., 2015. Introduction to the Red Sea: its origin, structure, and environment. In: The Red Sea. Springer, Berlin, Heidelberg, pp. 1–28.

Regorda, A., Spalla, M.I., Roda, M., Lardeaux, J.M., Marotta, A.M., 2021. Metamorphic facies and deformation fabrics diagnostic of subduction: Insights from 2D numerical models. Geochem. Geophys. Geosyst. 22 (10), e2021GC009899.

Reilinger, R., McClusky, S., ArRajehi, A., 2015. Geodetic constraints on the geodynamic evolution of the Red Sea. In: The Red Sea. Springer, Berlin, Heidelberg, pp. 135–149.

Richter, M.J., Brune, S., Riedl, S., Glerum, A., Neuharth, D., Strecker, M.R., 2021. Controls on asymmetric rift dynamics: Numerical modeling of strain localization and fault evolution in the Kenya Rift. Tectonics 40 (5), e2020TC006553.

Roda, M., Regorda, A., Spalla, M.I., Marotta, A.M., 2018. What drives Alpine Tethys opening? Clues from the review of geological data and model predictions. Geol. J. 54 (4), 2646–2664. https://doi.org/10.1002/gj.3316.

Rooney, T.O., Nelson, W.R., Dosso, L., Furman, T., Hanan, B., 2014. The role of continental lithosphere metasomes in the production of HIMU-like magmatism on the northeast African and Arabian plates. Geology 42 (5), 419–422. https://doi.org/10.1130/G35216.1.

Schettino, A., Ranalli, G., Fierro, E., Pierantoni, P.P., Zanoni, D., Turco, E., Rasul, N., 2019. Rift–drift transition in the Red Sea: a rheological model of the early stage of seafloor spreading. Geophys. J. Int. 217 (3), 1870–1893.

Schmeling, H., 2000. Partial melting and melt segregation in a convecting mantle. In: Physics and Chemistry of Partially Molten Rocks. Springer, Dordrecht, pp. 141–178.

Sewell, G., 1982. TWODEPEP, a small general purpose finite element program. Angew. Inform. 24 (4), 249–253.

Shinjo, R., Meshesha, D., Orihashi, Y., Haraguchi, S., Tamaki, K., 2015. Sr–Nd–Pb–Hf isotopic constraints on the diversity of magma sources beneath the Aden Ridge (Central Gulf of Aden) and plume–ridge interaction. J. Mineral. Petrol. Sci. 110 (3), 97–110. https://doi.org/10.2465/jmps.141211.

Shuler, A., Nettles, M., 2012. Earthquake source parameters for the 2010 western Gulf of Aden rifting episode. Geophys. J. Int. 190 (2), 1111–1122. https://doi.org/10.1111/j.1365-246X.2012.05529.x.

Thieulot, C., 2014. ELEFANT: a user-friendly multipurpose geodynamics code. Solid Earth Discuss. 6 (2), 1949–2096.

Thompson, D.A., Hammond, J.O.S., Kendall, J.M., Stuart, G.W., Helffrich, G.R., Keir, D., Ayele, A., Goitom, B., 2015. Hydrous upwelling across the mantle transition zone beneath the Afar Triple Junction. Geochem. Geophys. Geosyst. 16 (3), 834–846. https://doi.org/10.1002/2014GC005648.

Turner, S.P., George, R.M.M., Evans, P.J., Hawkesworth, C.J., Zellmer, G.F., 2000. Time-scales of magma formation, ascent and storage beneath subduction-zone volcanoes. Philos. Trans. R. Soc. Lond. 358 (1770), 1443–1464. https://doi.org/10.1098/rsta.2000.0598.

Watchorn, F., Nichols, G.J., Bosence, D.W.J., 1998. Rift-related sedimentation and stratigraphy, southern Yemen (Gulf of Aden). In: Sedimentation and Tectonics in Rift Basins Red Sea:-Gulf of Aden. Springer, Dordrecht, pp. 165–189.

Watremez, L., Leroy, S., Rouzo, S., d'Acremont, E., Unternehr, P., Ebinger, C., Lucazeau, F., Al-Lazki, A., 2011. The crustal structure of the North-Eastern Gulf of Aden continental margin: insights from wide-angle seismic data. Geophys. J. Int. 184 (2), 575–594. https://doi.org/10.1111/j.1365-246X.2010.04881.x.

Watremez, L., Burov, E., d'Acremont, E., Leroy, S., Huet, B., Le Pourhiet, L., Bellahsen, N., 2013. Buoyancy and localizing properties of continental mantle lithosphere: Insights from thermomechanical models of the eastern Gulf of Aden. Geochem. Geophys. Geosyst. 14 (8), 2800–2817. https://doi.org/10.1002/ggge.20179.

Wenker, S., Beaumont, C., 2018. Effects of lateral strength contrasts and inherited heterogeneities on necking and rifting of continents. Tectonophysics 746, 46–63.

Wessel, P., Smith, W.H., Scharroo, R., Luis, J., Wobbe, F., 2013. Generic mapping tools: improved version released. EOS Trans. Am. Geophys. Union 94 (45).